

TRANSFORMATIONS OF GALAXIES. II. GASDYNAMICS IN MERGING DISK GALAXIES

JOSHUA E. BARNES

Institute for Astronomy, University of Hawaii, 2680 Woodlawn Drive, Honolulu, HI; barnes@zeno.ifa.hawaii.edu

AND

LARS HERNQUIST¹

Board of Studies in Astronomy and Astrophysics, U.C. Santa Cruz, Santa Cruz, CA 95064; lars@helios.ucsc.edu

Received 1995 February 27; accepted 1995 October 3

ABSTRACT

In mergers of disk galaxies, gas plays a role quite out of proportion to its relatively modest contribution to the total mass. To study this behavior, we have included gasdynamics in self-consistent simulations of collisions between equal-mass disk galaxies. The large-scale dynamics of bridge- and tail-making, orbit decay, and merging are not much altered by the inclusion of a gaseous component. However, tidal forces during encounters cause otherwise stable disks to develop bars, and the gas in such barred disks, subjected to strong gravitational torques, flows toward the central regions where it may fuel the kiloparsec-scale starbursts seen in some interacting disk systems. Similar torques on the gas during the final stages of a collision yield massive gas concentrations in the cores of merger remnants, which may be plausibly identified with the molecular complexes seen in objects such as NGC 520 and Arp 220. This result appears insensitive to the detailed microphysics of the gas, provided that radiative cooling is permitted. The inflowing gas can dramatically alter the *stellar* morphology of a merger remnant, apparently by deepening the potential well and thereby changing the boundaries between the major orbital families.

Subject headings: galaxies: interactions — galaxies: structure — hydrodynamics — methods: numerical

1. INTRODUCTION

The various phases of the interstellar medium together comprise perhaps a tenth of the *luminous* mass of a typical disk galaxy and probably only a few percent of the *total* mass including the dark halo. Yet in many phenomena associated with galactic collisions, the gas plays a role quite out of proportion to its rather modest mass. Moreover, observations of atomic and molecular gas in interacting galaxies provide valuable information on the dynamical evolution of these systems. To understand the physical role of the gas, and to interpret the observations better, theoretical studies of gasdynamics in interacting galaxies are needed.

It was already apparent to Toomre & Toomre (1972) that violent tidal interactions might “bring *deep* into a galaxy a fairly *sudden* supply of fresh fuel,” and large-scale inflows of gas are clearly needed to explain the spectacular starbursts seen in some interacting systems (see, e.g., Joseph & Wright 1985). Such starbursts occur in circumnuclear “clouds” a few hundred parsecs in radius, which may contain $\gtrsim 10^{10} M_{\odot}$ of molecular gas (see, e.g., Solomon, Downes, & Radford 1992)—comparable to the *total* gas content of a pair of spiral galaxies. With star formation rates ~ 100 times those of normal galaxies, these clouds must be assembled on a rather short timescale (Larson 1987). Numerical simulations can shed some light on the dynamics of such rapid inflows.

Negroponte & White (1983) were the first to present self-consistent models of merging galaxies including a dissipative component composed of “sticky particles”; while they found large gas concentrations in the centers of their simulated remnants, the limited resolution of their calculations precluded a detailed analysis of the inflow dynamics.

Noguchi (1987, 1988) and Combes, Dupraz, & Gerin (1990) studied gas inflows in tidally perturbed disks, but these authors, unlike Negroponte & White, did not consider actual mergers. Using “smoothed particle hydrodynamics,” Hernquist (1989a, 1989b, 1991) showed that rapid gas inflows could be provoked by mergers between disk galaxies and intermediate-mass satellites (see also Mihos & Hernquist 1994a). More recently, we have run a self-consistent collision and merger of two gas-rich disk galaxies, producing a remnant containing a central gas cloud with a mass of $5 \times 10^9 M_{\odot}$ and a diameter of 200 pc (Barnes & Hernquist 1991, hereafter BH91).

While the general agreement between simulations using sticky and smoothed particles is encouraging, it should be emphasized that these techniques provide at best a schematic representation of the interstellar medium. In particular, it seems fair to say that existing calculations have only begun to test “star formation rules” (see, e.g., Noguchi & Ishibashi 1986; Olson & Kwan 1990a, 1990b; Mihos, Bothun, & Richstone 1993; Mihos & Hernquist 1994b, 1994c, 1994d), and there is also considerable uncertainty regarding the best ways to include “feedback effects” of star formation (see, e.g., Katz & Gunn 1991; Navarro & White 1993).

Instead of including such rules and effects, the present work employs the idealized models used in our earlier calculations (BH91; Hernquist & Barnes 1991; Barnes & Hernquist 1992) in which the ISM is simply represented as a compressible fluid. Like Barnes (1992, hereafter Paper I), we examine a small ensemble of parabolic encounters, varying the pericentric separation and orientations of the incoming disks. While gas collects in the central regions of all the merger remnants we have studied, we find some interesting sensitivity to the encounter parameters. To elucidate the physical mechanisms responsible for these rapid nuclear inflows, we also contrast models including heating and radi-

¹ Alfred P. Sloan Foundation Fellow, Presidential Faculty Fellow.

ative cooling with simpler calculations in which the gas is either held at a fixed temperature or is not allowed to cool radiatively.

This paper is organized as follows. Section 2 describes the methods we use to simulate galaxy collisions. In § 3 we examine the dynamical evolution of our models, focusing first on their overall behavior and then on the details of the gas response. In § 4 we describe the structure of the resulting merger remnants and the distribution and kinematics of the gas within them. Finally, in § 5 we offer a summary and a discussion of our results. Details of the model and numerical implementation are covered in Appendix A, and brief descriptions of the video sequences that are related to this paper and that will appear on a later *Astrophysical Journal* videotape are given in Appendix B.

2. ENCOUNTER MODELS

The disk galaxies we model contain three types of matter: stars, dark matter, and interstellar gas. We assume that the collisionless Boltzmann equation describes the evolution of the stars and dark matter; this is fairly uncontroversial, given the large number of stars making up a typical galaxy and in view of prevailing assumptions about the nature of the dark matter. We assume that the gas can be modeled by the standard laws for a compressible fluid, with the addition of gravitational forces, radiative cooling, and shock heating. This assumption is somewhat suspect since the gas in disk galaxies occurs in a variety of phases, and the energy densities in magnetic fields and cosmic rays are comparable to the thermal energy density of the gas itself. But while the interstellar material *clearly* does not behave like an ideal gas on parsec scales, we argue that our approach should do a good job of representing the overall dynamics of the gas on scales of several hundred parsecs. Finally, we use Poisson's equation to obtain the gravitational field generated by the stars, dark matter, and gas. Details of our physical model and the numerical methods we use to implement it are discussed in Appendix A. In brief, we employ a hierarchical N -body method to simulate the collisionless components and smoothed particle hydrodynamics (SPH) to simulate the gas; thus, all components are represented with particles, which considerably simplifies the construction of the code and the analysis of the results.

2.1. Gas in Bulge/Disk/Halo Galaxy Models

The model galaxies used in the present study are similar to the bulge/disk/halo models used in Paper I, which were designed to approximate a Bahcall & Soneira (1980) model of the Milky Way. The disks have an exponential distribution in cylindrical radius and an isothermal profile perpendicular to the disk plane; they are embedded in dark halos and contain compact bulges, each of which would have a King model profile in isolation (King 1966). Construction of the spheroidal components and realization of the disk component follows the procedure described in Paper I. Following Hernquist (1989a, 1989b), the gas is distributed with the same radial and vertical density profile as the disk stars. In all cases presented here, the bulge to disk to halo mass ratio is 1:3:16, and the gas amounts to 10% of the disk mass.

Because we include nongravitational processes such as radiative cooling, we do not have the freedom to rescale our models to any system of units with the same gravitational constant; on the contrary, we are obliged to adopt a definite physical system of units. For ease of comparison with Paper

I, we take our units of length, mass, and time to be 40 kpc, $2.2 \times 10^{11} M_{\odot}$, and 250 Myr, respectively (implying $G \equiv 1$), and assign our galaxy models a disk scale length of 1/12 and a total mass of 1.25. The total binding energy of our adopted galaxy model is $E = -1.408$ model units. In physical terms, this galaxy model has a disk scale length of 3.33 kpc, a luminous mass of $5.5 \times 10^{10} M_{\odot}$, and a total mass of $2.75 \times 10^{11} M_{\odot}$, roughly matching the parameters of the Milky Way.

Radiative cooling is implemented using a standard solar abundance cooling curve. Since cooling is quite rapid at the relevant densities and temperatures, we are obliged to cut off radiative cooling at temperatures below 10^4 K; otherwise, the gas fragments into small and extremely dense clumps. In real galaxies, such thermal instabilities presumably result in star formation, which in turn reheats some of the gas and thereby establishes a multiphase ISM. Our models do not include these effects, and we view the adopted cutoff as a compromise that forces the simulated gas to approximate the warm ISM of a real galaxy.

2.2. Evolution of an Isolated Disk Galaxy

Figure 1 presents separate views of the gas and stars in an isolated galaxy model. This simulation used 8192 particles to represent the gas, 4096 to represent the bulge, 16,384 to represent the stellar disk, and another 16,384 to represent the halo. Gravity was "softened" using a spline kernel (Hernquist & Katz 1989) with a softening parameter $\epsilon = 0.015$ length units. The force calculation tolerance and integration time step were chosen such that total energy and angular momentum varied by approximately 0.02% and 0.1%, respectively, over the course of the simulation. Given other uncertainties and sources of error—in particular, those due to effects of finite particle number—it seems unlikely that such inaccuracies will have significant consequences for these experiments.

The transient spiral structure seen in this simulation is typical of disk galaxy models evolved in isolation. Such spiral patterns are usually attributed to swing amplification of discreteness noise in the N -body representation of the mass distribution (see, e.g., Toomre 1981, 1990), though global dynamics may also play a role (see, e.g., Sellwood 1989). A result of this spiral making is that purely stellar disk models suffer irreversible dynamical heating that suppresses the swing amplifier after a few rotation periods (see, e.g., Sellwood & Carlberg 1984). The gas yields a better defined spiral pattern than the stars because radiative cooling in the gas damps its random velocities; dissipation thus permits disks consisting of both gas and stars to maintain spiral structure over longer timescales (see, e.g., Carlberg & Freedman 1985; Hernquist 1990a). However, the relationship between the spirals seen here and those observed in actual galaxies is problematic because discreteness noise due to the *stellar* components of real galaxies is negligibly small. Other sources of fluctuations, such as molecular cloud complexes, may seed the spiral patterns of real galaxies.

But as the above discussion already implies, the *dissipative* nature of the gas, which comes into play in maintaining spiral structure, must also lead to irreversible evolution. Figure 2 presents evidence for such evolution in the model just depicted. The descending line shows the net change in binding energy due to radiative losses, while the two rising curves represent gas fractions above densities of

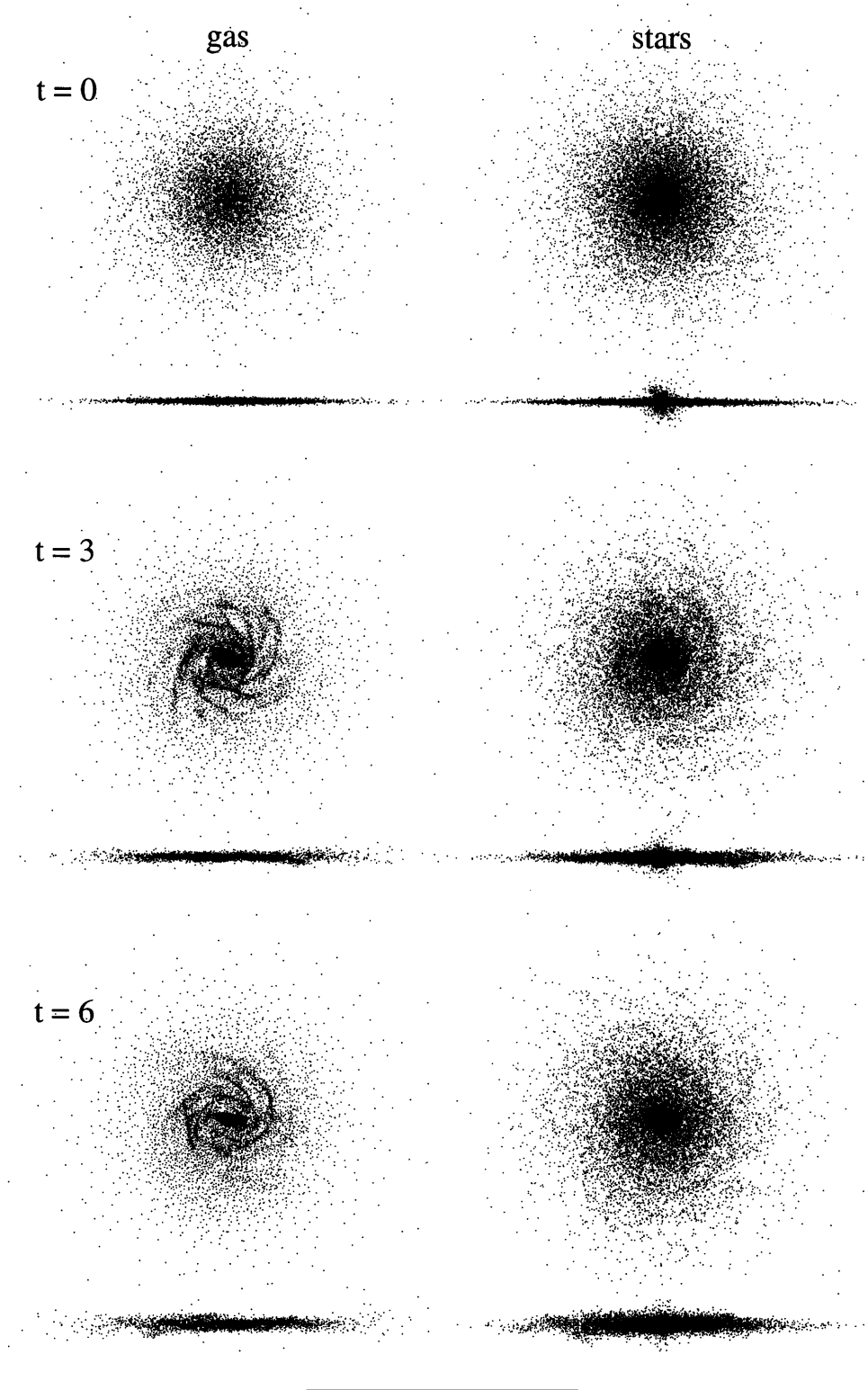


FIG. 1.—Evolution of a single disk galaxy. On the left is the gas, shown both face-on and edge-on, while on the right are similar views of the disk and bulge particles. Times since the start of the simulation are indicated, and the scale bar at the bottom is 1 unit long. The transient spiral patterns seen as the disk evolves are plausibly attributed to swing amplification of $N^{1/2}$ noise, while the somewhat elongated distribution of gas in the center of the $t = 6$ disk hints at the presence of a slowly growing instability.

10^2 and $10^{2.5}$, with one density unit corresponding to $0.0034 M_{\odot} \text{ pc}^{-3} \simeq 0.1 \text{ cm}^{-3}$. There is an initial transient lasting about 0.1 time units, during which the gas collapses vertically to a scale height less than half that of the stars. After this, the system dissipates very slowly, losing $\sim 0.1\%$

of its binding energy per time unit and gradually increasing its gas fraction at $\rho > 10^2$. At later times ($t \gtrsim 4.0$), the disk develops a weak bar, which results in a slightly higher dissipation rate and an increasing gas fraction at $\rho > 10^{2.5}$. Nonetheless, these changes are *much* smaller than the

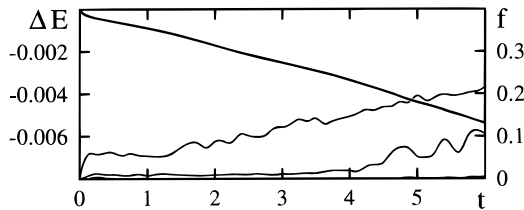


FIG. 2.—Energy dissipation and density evolution for the isolated disk model shown in Fig. 1. The descending curve shows the change in binding energy due to dissipation; radiative losses amount to only one part in $\sim 10^3$ of the total binding energy per dynamical time. The rising curves show gas fractions above densities of $\rho = 10^2$ and $10^{2.5}$; these slowly increase as a result of dissipative evolution. This plot shows that any instabilities in this isolated disk model produce only gradual changes.

changes produced in collisions, which implies that these initial disks are close enough to stable equilibria to be useful in simulations.

2.3. Encounter Parameters

Following earlier studies (Barnes 1988; Paper I), we focus on relatively close parabolic encounters between equal-mass bulge/disk/halo galaxies; such encounters typically result in mergers after one or two orbits. This focus is motivated partly by computational limitations—wider encounters take longer to merge and thus are more costly to simulate—but also by observations that indicate that the most luminous starbursts occur in violently interacting and merging systems (see, e.g., Joseph & Wright 1985; Sanders et al. 1988a, 1988b).

Parameters for the encounters studied are listed in Table 1. Here R_p is the pericentric separation the two galaxies would reach if they continued precisely along their initial parabolic orbits; in every case, the initial orbit was set up so as to reach this point at time $t_p = 1$. Angles i_1 , ω_1 and i_2 , ω_2 specify the initial orientations of the two disks, following the definition used by Toomre & Toomre (1972). Hence, in encounter A, the $i = 0$ disk has its spin axis aligned with the orbital angular momentum vector, while its counterpart is tipped by 71° . Encounter 1 is a repeat of encounter A with half as many particles, and encounter 2 is derived from encounter 1 by exchanging the two galaxies and reversing their spins. Encounters 3 and 4 are wider passages, both involving inclined disks with antiparallel spin vectors.

To assess the physical nature of the mechanisms responsible for separating the stars and gas, we ran other models where we varied the gas physics. In encounter 1_A , we disabled radiative processes, so that the internal energy of the gas was changed only by adiabatic heating and cooling and by entropy generation in shocks. In encounter 1_I , an isothermal equation of state was employed so that the gas

was forced to remain at its initial temperature of 10^4 K. This latter choice mocks the more detailed treatment of radiative heating and cooling in encounter A, for example, in which the gas can reside at any temperature but tends to hover near 10^4 K. Not listed in Table 1 are several additional runs in which we varied the artificial viscosity parameters.

Finally, we ran encounter A_0 using the same initial conditions as encounter A, but treating all particles as collisionless. This encounter may be closely compared with its gasdynamical analog, since all particles were started with exactly the same positions and velocities. We will also compare these calculations with encounter A of Paper I, hereafter identified as encounter A_1 , which describes the same physical situation as encounter A_0 but was run with Plummer softening instead of the spline softening used here; numerical tests indicate that the old calculation offers about half the spatial resolution of the newer runs. Likewise, encounters 1, 2, 3, and 4 of this paper resemble encounters 1, 4, 7, and 6 described in Paper I.

3. COLLISION DYNAMICS

To illustrate the dynamics of a typical collision, we present results from encounter A in some detail. Section 1 of the videotape and Figures 3 and 4 show the evolution of this system viewed from a direction normal to the orbital plane. The video shows *all* components of the simulation: dark matter in red, bulge stars in yellow, disk stars in blue-white, and gas in green; the two figures show the gas and the disk stars, respectively. The smooth curves in the initial frames show the parabolic trajectories the two galaxies would follow were they simple point masses.

On the whole, the early evolution of this encounter is very similar to the corresponding encounter of Paper I—a result scarcely surprising in view of the fact that gas makes up only 1.5% of the total mass. Before their first passage, the disks develop spiral patterns just like those in isolated disks. Violent tidal forces at first pericenter ($t = 1$) distort both galaxies; the direct disk shows the resulting features to maximum advantage since it couples most effectively to the tidal disturbance and is moreover seen face-on in this projection. Of particular interest are differences between the distributions of gas and stars. For example, at $t = 1.125$, the region between the two disks is nearly devoid of stars but contains a significant amount of gas. This material was ram-pressure stripped from the disks during the collision; some of it probably came from the tip of the bridge arm extending from the direct disk, which is largely bereft of gas.

Subsequently, this arm extends toward the other galaxy, and by $t = 1.5$, it has bridged the gap, pouring gas and stars onto the inclined disk. At later times, the stellar debris from this bridge forms a broad fan-shaped structure immediately to the right of this disk; this feature is reminiscent of those seen in simulations of shell formation in elliptical galaxies (see, e.g., Hernquist & Quinn 1988, 1989; compare, for example, with Fig. 1 from Hernquist & Quinn 1988). Analogous structures are also visible in the stellar-dynamical encounters of Paper I. The gas, on the other hand, is unable to penetrate the inclined disk, as illustrated in section 2 of the videotape. Such separation of gas and stars in intersecting flows produces a number of gas-poor shells and plumes in these simulations (see also Hernquist & Weil 1992).

These views display to advantage the tidal tails launched from the disks at first passage. Here again the gas may produce crisper and better defined structures than the stars.

TABLE 1
EQUAL-MASS PARABOLIC ENCOUNTERS

Model	R_p	i_1	ω_1	i_2	ω_2	N	Remarks
A	0.2	71	30	0	...	90112	See BH91
A_0	0.2	71	30	0	...	90112	Pure N -body run
1	0.2	71	30	0	...	45056	Half as many particles
1_I	0.2	71	30	0	...	45056	Isothermal (10^4 K)
1_A	0.2	71	30	0	...	45056	No radiative cooling
2	0.2	180	...	109	30	45056	Disk spins reversed
3	0.4	71	-30	109	-30	45056	Wider encounter
4	0.4	71	90	109	90	45056	Nearly polar passages

NOTE.— R_p is the pericentric separation, angles i_1 , ω_1 and i_2 , ω_2 specify the orientations of the disks, and N is the total number of particles.

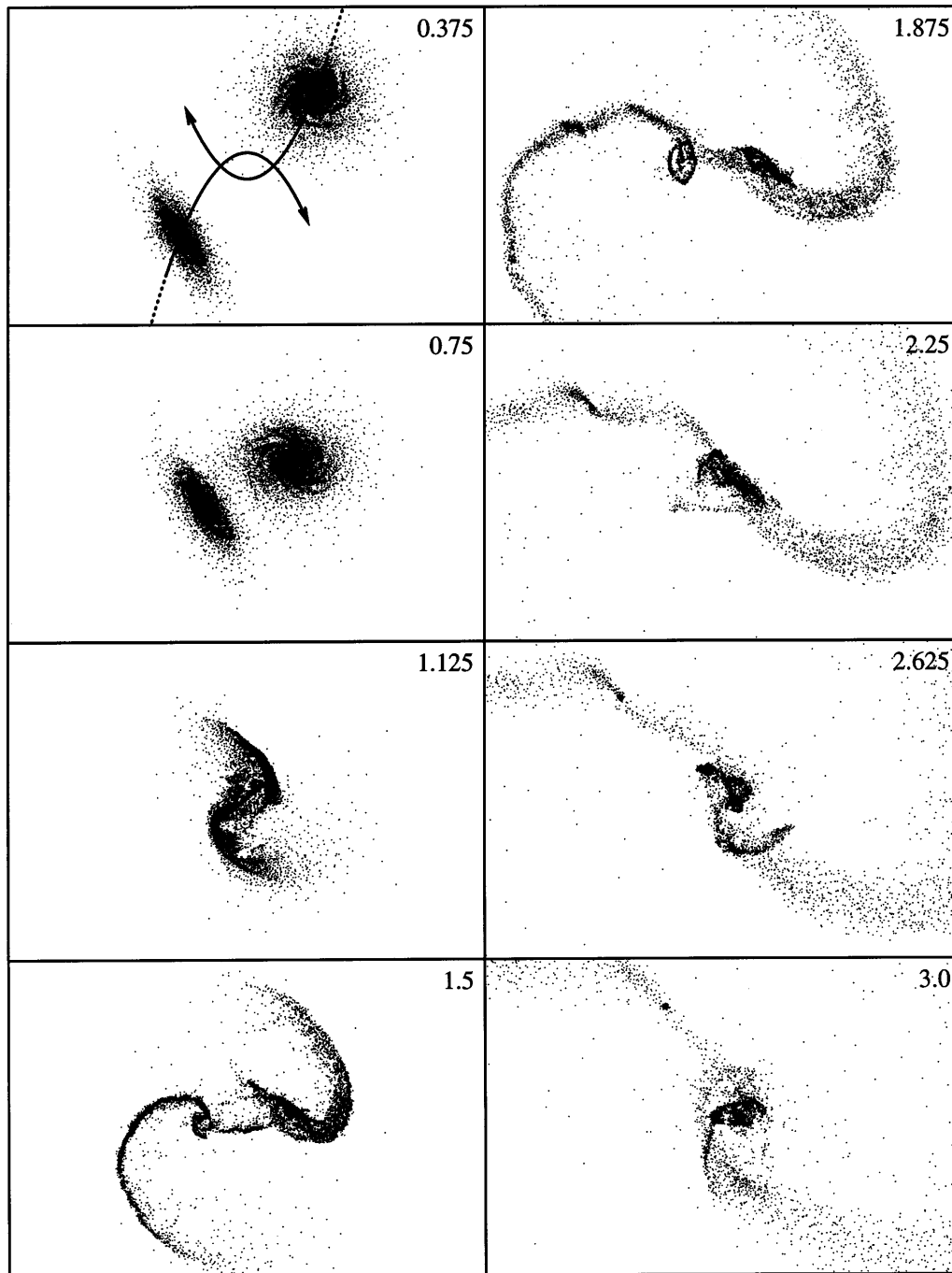


FIG. 3.—Evolution of the gas distribution in encounter A, projected onto the orbital plane. These frames are 3.6×2.4 length units; elapsed time is shown at the upper right of each. The first frame also shows the projected parabolic orbits of the infalling galaxies.

The gas in the left-hand tail is concentrated into a remarkably thin filament running along the ridge line of the stellar distribution by the self-intersection of the flow in this violently perturbed disk. From the views in Figure 3 at time $t = 1.5$, it appears that the gas intersects simultaneously along most of the length of this tail, an impression strengthened by reviewing section 2 of the videotape. The right-hand tail does not produce quite as narrow a filament, perhaps because the out-of-plane forces experienced by the inclined disk during first pericenter make the gas flow less likely to self-intersect. In this case, the point of maximum gas density appears to propagate outward along the tail (see, Wallin 1990).

As in the collisionless simulations of Paper I, the orbital decay of this system is governed by gravitational braking. This point is illustrated in Figure 5, which plots the specific angular momentum of the bulge particles in encounters A, 1, 2, 3, and 4 and compares these to the corresponding collisionless simulations. By and large, the orbit decay rates are little affected by gas; the one possible exception is the retrograde and deeply interpenetrating passage of encounter 2, which seems likely to give rise to some gasdynamic drag and does in fact decay somewhat more rapidly than its collisionless counterpart.

Because of this gravitational braking, the galaxies in encounter A begin to fall back together around $t = 1.6$.

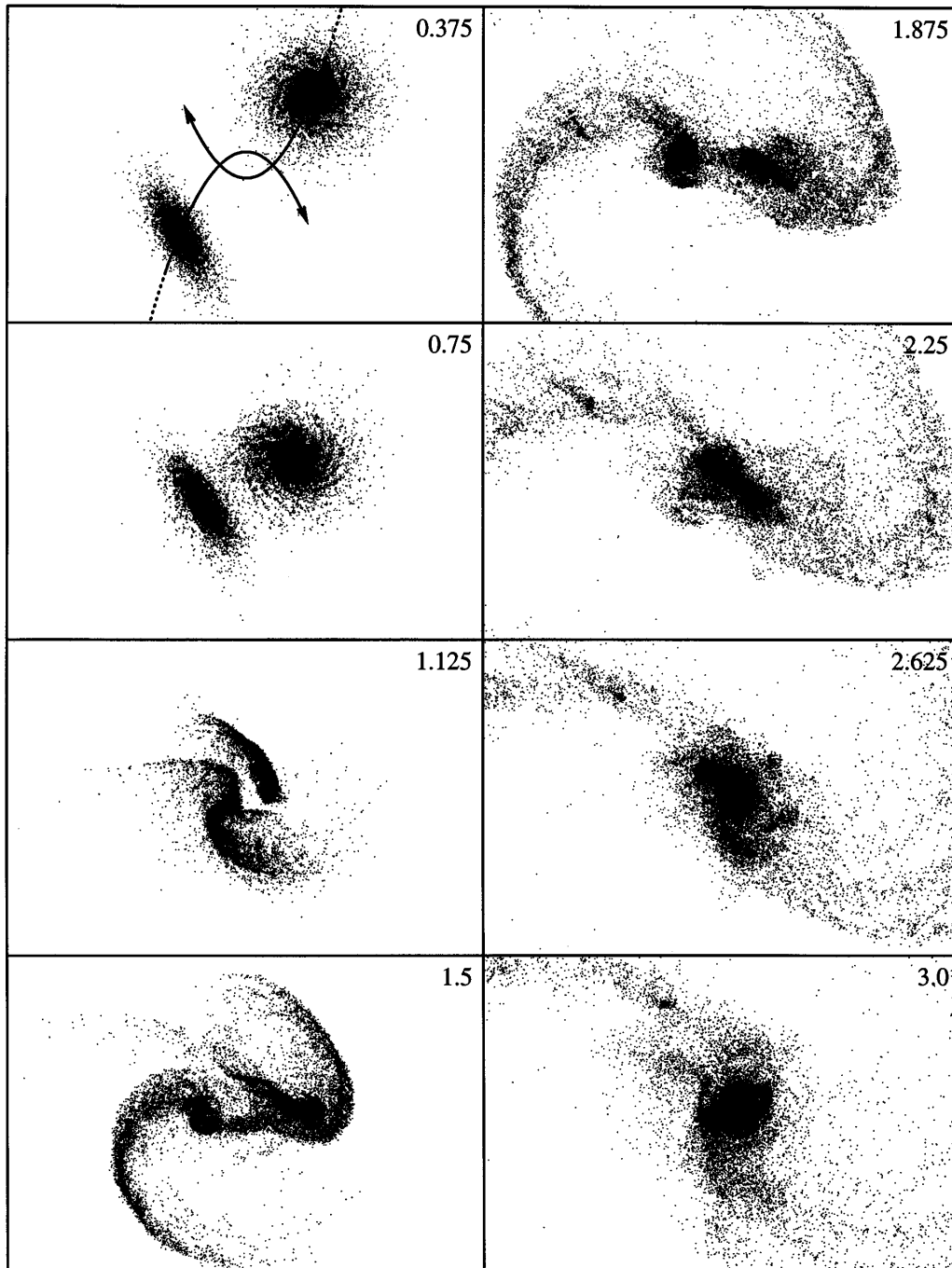


FIG. 4.—Evolution of the stellar distribution in encounter A, projected onto the orbital plane. The scale is the same as in Fig. 3.

After $t = 2.25$, it is no longer clear if we are dealing with two galaxies or with one galaxy containing two nuclei; nonetheless, much additional evolution must take place before the merger is completed, and various substructures are present at later times. Indeed, the irregular nature of the stellar component at $t = 2.625$ is reminiscent of transient structures seen in objects formed through dissipationless collapse from cosmological initial conditions (see, e.g., Dubinski & Carlberg 1991). Much of this substructure has faded by the final frame at $t = 3$, though clearly the remnant has not reached a fully relaxed configuration.

It is interesting to compare the stellar component this model with its analog from Paper I. Spiral structure of even the *stellar* disks shown in Figure 4 is crisper than that seen

in Figure 1 of Paper I, evidently because the gas reduces the overall Q of the system. In addition, the irregular substructure visible in the last frames of Figure 4 is much less well defined in the corresponding experiment of Paper I. But not every feature is better defined in the present calculations; for example, the shell-like structures due to material following along the bridge connecting the two galaxies seem more diffuse here than in the purely stellar-dynamical version.

3.1. Thermodynamic Indicators

Following the format of Figure 2, Figure 6 presents radiative energy losses and density evolution for encounters A, 2, 3, and 4 (encounter 1 is not shown because some files were lost, but the available data indicate that this case is similar

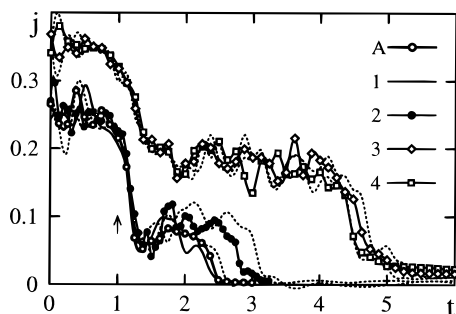


FIG. 5.—Specific angular momentum of bulge material, plotted as a function of time. Results are shown for encounters A, 1, 2, 3, and 4 (solid lines and symbols) and for corresponding encounters from Paper I (dotted lines). The arrow indicates first pericenter for all encounters.

to encounter A). All of these collisions lead to rather dramatic radiative losses, with peak dissipation rates during close passages nearly 3 orders of magnitude greater than the gradual radiative energy losses experienced by isolated disks. The most dissipative, encounter 2, loses in total some 14% of its initial binding energy; the other encounters lose nearly as much. Such losses are almost an order of magnitude *greater* than the rotational kinetic energy of the gas in the original disks; clearly, most of the energy radiated is gravitational energy released as gas falls into—and helps create—deep potential wells.

The closer encounters (A and 2) exhibit rather high dissipation rates on their first passages, due largely to direct hydrodynamic interactions between the gas disks. After these first passages, gas fractions at densities $\rho \gtrsim 100$ –1000 model units rise dramatically; encounters A and 1 also develop significant amounts of gas at densities above 10^4 , while encounter 2, with its retrograde disks, does not. Subsequent passages, which swiftly culminate in merging of the galaxies involved, produce significant energy losses and dramatic increases in gas fractions at $\rho \gtrsim 10^4$; after these mergers are complete, dissipation rates drop quickly as equilibrium is reached.

The wider encounters in Figure 6 initially show more gradual evolution. Although the first passages of these systems produce readily detected tidal features, including striking examples of bridges, tails, spirals, and bars, they do not trigger the large energy losses seen in the closer passages. In encounter 3, the gas in both disks becomes centrally concentrated as a result of tidal evolution; consequently, this system suffers almost no radiative losses on second passage at $t \simeq 4.4$ but dissipates rapidly during the final encounter and merger at $t \simeq 5.2$. The nearly polar first passage of encounter 4, in contrast, provokes only a very modest increase in gas densities, and as a result these still-extended gas disks undergo violent hydrodynamic interactions starting with their second passage at $t \simeq 4.3$.

All four encounters eventually produce merger remnants with gas fractions of 60%–80% at densities of $\rho \gtrsim 10^4$ model units ($\sim 10^3 \text{ cm}^{-3}$), but the rate of density increase clearly depends on the initial parameters of the encounter. Thus, if starbursts are hypothesized to occur only when significant amounts of gas are assembled at densities above 10^3 cm^{-3} , encounters A and 1 would produce starbursts while the galaxies involved were still reasonably distinct, while the other encounters would not develop starbursts until the galaxies actually merged.

3.2. Disk Response

To account for the dramatic increases in gas density just described, we examine the dynamical evolution of the strongly perturbed disks of encounter A. Both disks develop pronounced bars in response to the strong tidal forcing they experience at pericenter, an effect already emphasized by Noguchi (1987, 1988) and BH91. Section 3 of the videotape shows the formation of a bar in the direct disk of encounter A, using the same color scheme as in section 1; Figure 7 compares the gas and stellar structure of both disks. Note that the bar in the direct disk develops more rapidly than the one in its inclined counterpart; compare, for example, the appearance of the former at $t = 1.375$ with the latter at $t = 1.75$.

These bars are responsible for several striking evolutionary changes in their parent disks. As in previous studies (see, e.g., Schwarz 1984), ringlike structures with diameters comparable to the lengths of the bars form in both the stellar (see section 5 of the videotape accompanying Paper I) and gaseous distributions. Figure 7 suggests that these “ Θ -shaped” features are actually tightly wound spirals extending from, and presumably driven by, the stellar bars. Again, the kinematically cold gas exhibits a stronger response to the bar forcing than the stellar component does. The particles making up these features come largely from radii outside the circumference of the bars themselves. A different fate awaits the gas particles initially lying within the bar’s sweep; they become concentrated within a gaseous bar, aligned roughly with the stellar bar, which then contracts toward the center of the disk.

Tidally induced bars also form in encounters A_0 and A_1 , although they are not identical to the bars illustrated here. For example, the average pattern speed of the bar in the direct disk of encounter A is ~ 5.7 radians per time unit, while the corresponding bars in encounter A_0 and A_1 have pattern speeds of ~ 3.9 and ~ 3.2 radians per time unit, respectively. It is not clear why the bar in encounter A turns more rapidly; one possibility is that gas inflow toward the center of this disk deepens the potential well and that the deeper well implies a higher pattern speed. This suggestion is consistent with the smaller difference noted between encounters A_0 and A_1 , since the latter has a shallower potential well because of its poorer spatial resolution.

3.3. Gas Inflow in Disks

As hinted above, the gas and stars do not have the same response to tidal forcing. In both disks pictured in Figure 7, the gas bar is slightly out of phase with the stellar bar, leading it by an angle of 5° – 10° . This is easily seen in the direct disk at $t = 1.375$, where the gas bar leads the stellar bar by $\sim 5^\circ$; a similar difference can be seen in the inclined disk between $t = 1.5$ and $t = 1.75$. As noted previously (BH91), such phase differences between the gas and the stars give rise to torques that remove angular momentum from the gas. This process is quite efficient at driving gas toward the center of a barred disk. Section 3 of the videotape shows the resulting oval ring of gas quite clearly; note that the orbits of gas particles remain parallel to the bar.

Evidence for the dominant role of gravitational torques in this process is presented in Figure 8. Here, the top panel shows the specific angular momentum, j , of the Lagrangian volume of gas which has collected within a radius of 0.03 length units of the center of the direct disk at time $t = 1.75$. Initially, most of this gas lies within 0.1 length units of the

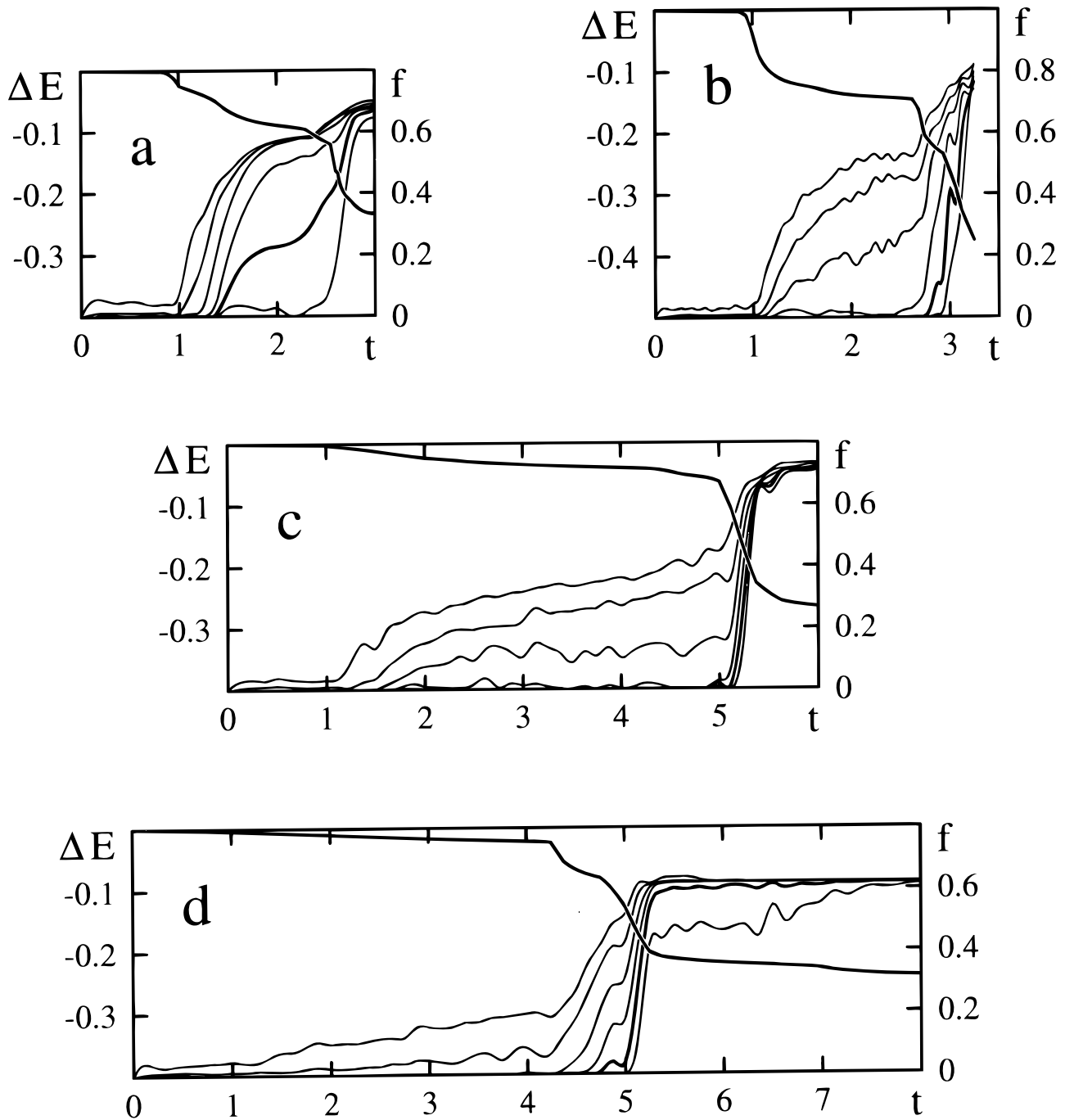


FIG. 6.—Energy dissipation and density evolution for various encounters. Each frame follows the format of Fig. 2, but the scale used for radiative losses, shown by the descending curves, is a factor of 50 greater. The ascending curves show gas fractions above densities $\rho = 10^2, 10^{2.5}, 10^3, 10^{3.5}, 10^4$, and $10^{4.5}$; a heavy line is used for the gas above $\rho = 10^4$ (approximately 10^3 cm^{-3}). Results are shown for (a) encounter A ($R_p = 0.2$, direct), (b) encounter 2 ($R_p = 0.2$, retrograde), (c) encounter 3 ($R_p = 0.4$, inclined), and (d) encounter 4 ($R_p = 0.4$, polar).

center, but a portion comes from a leading two-armed spiral that extends several times farther out, and this outlying gas contains a good fraction of the initial angular momentum. During the time interval shown in this figure, the total angular momentum of the gas declines by a factor of ~ 30 . The rate of change of j with respect to time, dj/dt , found by numerical differentiation of the curve in the upper panel, is plotted as a smooth curve in the middle panel of Figure 8. Also plotted as filled and open circles, respectively, are the gravitational and gasdynamic torques acting on this gas. The close agreement between dj/dt and the gravitational torque makes it quite clear that the angular momentum of

the gas is being extracted *gravitationally*. Only near first pericenter are nongravitational torques noticeable, and the sign of these torques implies that angular momentum is being *added* to the gas. At other times, the rather small discrepancies between the gravitational torque and dj/dt are probably due to numerical approximations in evaluating the latter.

The origin of the gravitational torque is examined in more detail in the bottom panel of Figure 8. Here, the dashed and dotted lines represent the torques on the gas due to the gravitational fields of the halo and disk, respectively, while the solid line represents the torque exerted by

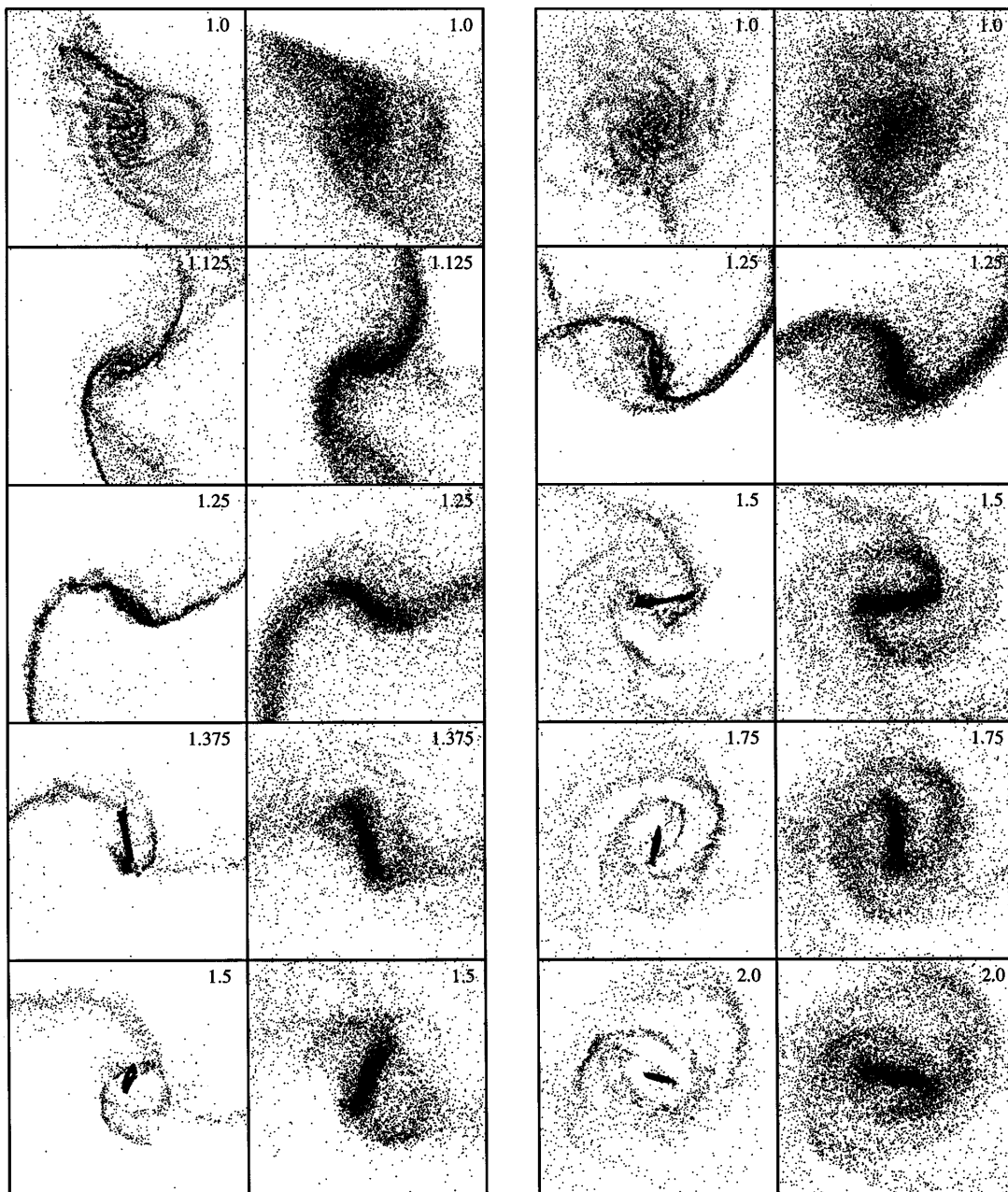


FIG. 7.—Close-ups of the two disks in encounter A, comparing the gas and stellar distributions. Each frame is 0.5×0.5 length units. The left-hand series shows the direct disk, while the right-hand series shows the inclined disk.

the other galaxy. Up until first passage ($t = 1$), most of the torque is provided by the gravitational field of the other galaxy; angular momentum is transferred from the spin of this disk to the relative orbit of the two galaxies. As the galaxies pass each other, this part of the torque changes sign, but now the total torque is dominated by transfer of angular momentum from the gas to the stellar disk due to the phase difference between the stellar and gaseous bars described above, and the spin-down of the gas continues.

Compared with its direct companion, the inclined disk in encounter A is not perturbed quite so strongly and hence evolves in a more gradual fashion. An analysis of the gas-dynamics in this disk is complicated by the direct transfer of gas along the tidal bridge connecting the galaxies. Nonetheless, by time $t = 2$, most of the gas in this disk has also contracted into a thin elongated bar. The dynamical mecha-

nism causing this inflow appears to be the same as in the direct disk.

The violent inflows we observe in these strongly perturbed disks do not depend on numerical details such as the treatment of artificial viscosity; we varied the viscosity parameters α and β by factors of 3 in each direction and tried an alternate form for the artificial viscosity (§ A2), all with no appreciable effect. We likewise observed rapid inflows in encounter 1₁, where the gas temperature was fixed at 10^4 K.

On the other hand, the relative orbit and orientation of the disks clearly affects the strength and speed of the gas inflows; wider and/or more highly inclined encounters produce slower inflows. The structure of the victim galaxy models may also influence the inflow rate; models with rapidly rising rotation curves are not so likely to form bars

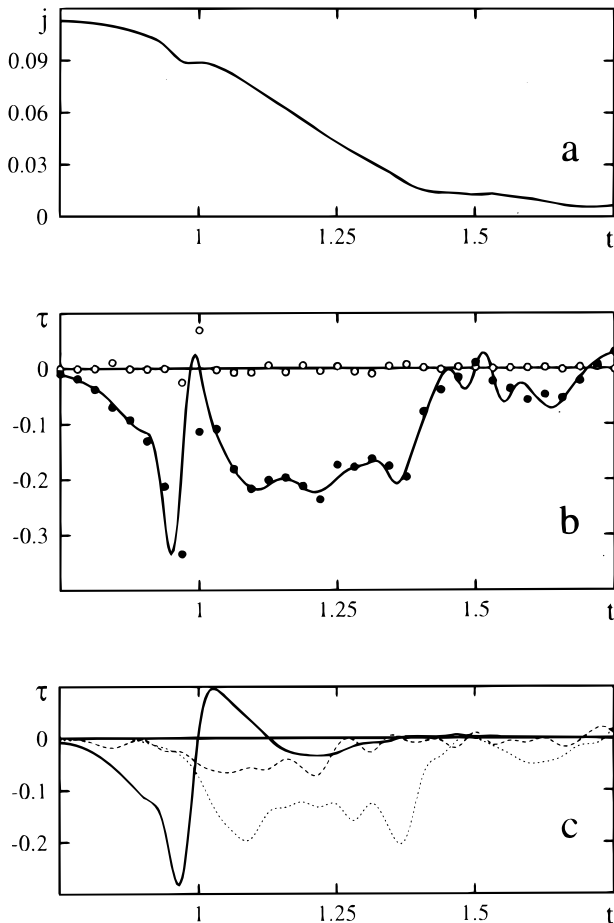


FIG. 8.—(a) Specific angular momentum of the gas that collects at the center of the direct disk in encounter A, plotted as a function of time. (b) Specific torques acting on this gas. Here the smooth curve is obtained by numerically differentiating the curve plotted in the panel above. Filled circles are gravitational torques exerted on the gas by the rest of the system, while open circles are torques due to hydrodynamic forces. (c) Components of the gravitational torque; the solid line is the torque due to the other galaxy, the dashed line is the torque due to the halo, and the dotted line is the torque due to the disk and bar.

and thus experience slower inflow (see, e.g., Mihos & Hernquist 1994a, 1994b). Nor can we rule out the possibility that faster, nonmerging collisions can also trigger gas inflows in disk galaxies (Noguchi 1987, 1988).

3.4. Final Passages

The galaxies in these encounters undergo a series of ever-closer passages before finally merging. Section 4 of the videotape and Figure 9 illustrate the behavior of the gas in the later passages of encounter A. As in section 2 of the videotape, gas from the inclined disk is colored red, while that from its direct companion is shown in green. The orange color of the ring in the inclined disk reflects the fact that roughly one-quarter of the mass in this ring was originally part of the other galaxy. The two rings of gas, which track the centers of their parent galaxies, come within ~ 0.04 length units of each other on their second passage and suffer a head-on collision the third time around. Between $t = 2.25$ and 2.5 , the angular momentum of their relative orbit falls by an order of magnitude; such rapid orbit decay is a consequence of the efficient transport of orbital angular momentum from these tightly bound

objects to the surrounding material (see, e.g., Barnes 1988; Paper I).

The evolution of the spin angular momenta of these two rings is quite complex. The ring in the inclined disk, seen at the lower right in the first frame of Figure 9, spins about an axis inclined by nearly 90° to the orbital axis. This ring appears quite small in the next few frames merely because we are viewing it nearly end-on. Between times $t = 2.25$ and 2.5 , the net spin of this ring remains fairly constant, but torques exerted during the second passage slew the spin axis counterclockwise, as viewed in this projection, by roughly 45° . The direct ring spins about an axis almost parallel to the orbital axis. During the second passage, the spin of this ring nearly doubles, and the ring expands into the more open form seen at time $t = 2.343$. Subsequently, however, gravitational torques appear to remove much of this angular momentum; by $t = 2.531$, it has fallen to less than one-quarter of what it was at $t = 2.25$, and the ring has closed up to become the narrow linear structure seen at the bottom of this frame.

Thus, when these two rings finally encounter one another directly on their third passage, they have lost much of the orbital and spin angular momentum that they originally possessed. This third passage produces a dramatic gas-dynamic interaction between the two galaxies. Efficient radiative cooling keeps the gas quite close to the cutoff temperature of 10^4 K even as the two rings collide at ~ 500 km s $^{-1}$; this accounts for the rapid energy loss seen in the first panel of Figure 6 just after time $t \simeq 2.5$. But as section 4 of the videotape and Figure 9 show, not *all* of the rings' kinetic energy is dissipated instantly; although much of their relative velocity cancels out, the rings manage to separate partly before falling back together and finally coalescing.

In contrast to merger of the highly concentrated gas rings just described, Figure 10 shows the later passages and merger of the rather unevolved gas disks in encounter 4. This figure closely corresponds to Figure 9 of Paper I, with three differences: first, despite employing similar initial orbits, the present encounter 4 merges about 0.25 time units before encounter B of Paper I; second, here the gas is shown rather than stars; and third, the view is progressively expanded from time $t = 5$ on. Because they were only gently perturbed on their first passage, these gas disks are still relatively extended at their next encounter. The rapid evolution of the gas is driven both by gravitational interactions, as already seen in encounter A, and by direct hydrodynamic interactions, commencing with a nearly face-on collision at $t \simeq 4.3$. While a plume of shocked gas connects the galaxies at $t = 4.5$, a careful comparison with the collisionless version of Paper I suggests that much of the disk gas is left in place after this passage; evidently, the gas distributions in these two disks are inhomogeneous enough to partly avoid one another in a face-on meeting. However, the *tidal* effects of this passage are dramatic, triggering enough inflow to collect more than half of each galaxy's gas into its core.

4. MERGER REMNANTS

As Figure 6 reports, gas densities rise throughout the encounters and level off after the galaxies finally merge. Long-term simulation of such merger remnants is expensive because gas particles in the high-density regions must take small time steps to satisfy the Courant condition (see § A4). Moreover, it is unlikely that even such expensive calcu-

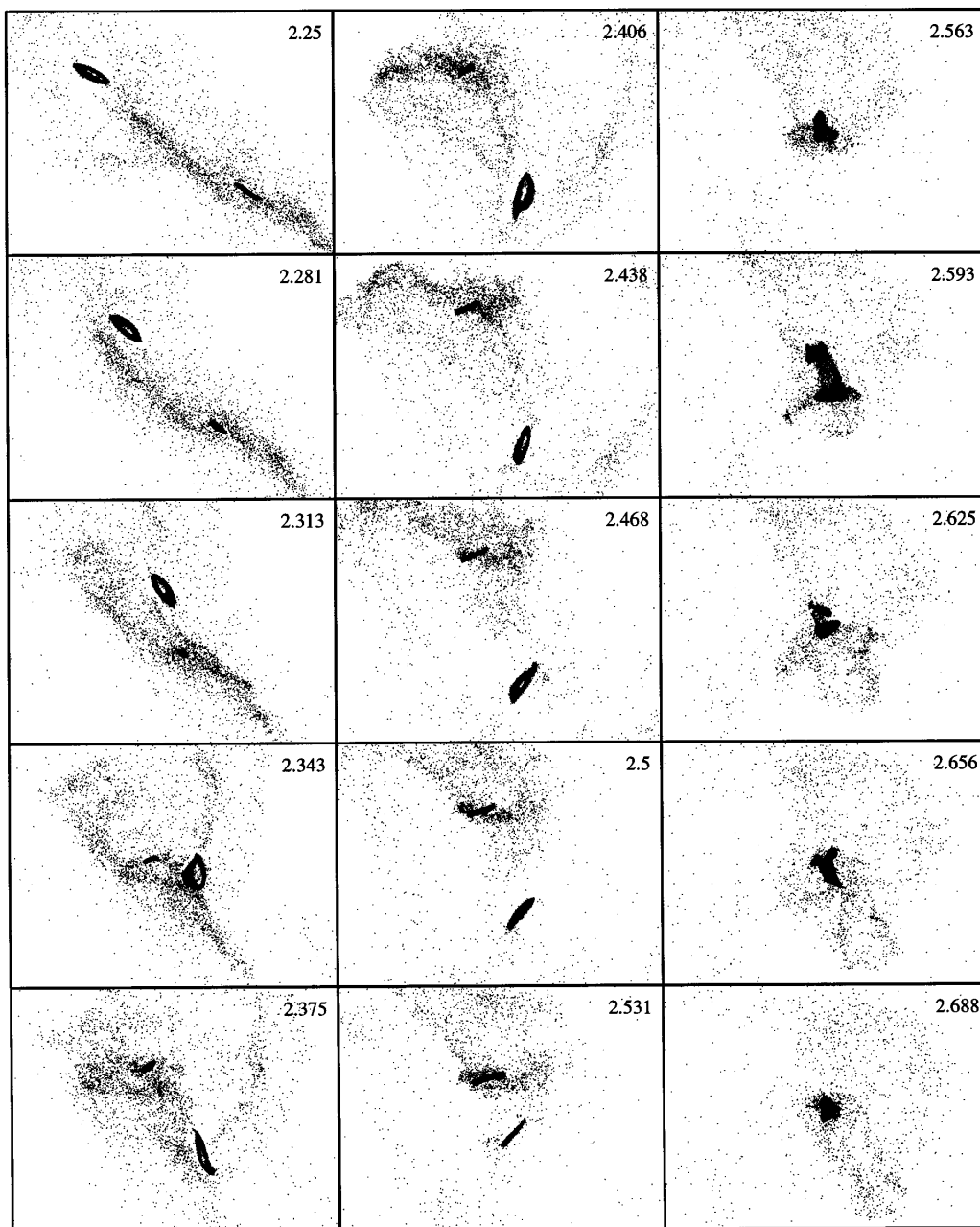


FIG. 9.—Evolution of the gas distribution during the final passages of encounter A, projected onto the orbital plane. All frames are 0.4×0.3 length units, with elapsed times as shown.

lations could reproduce accurately the evolution of the high-density gas for many tens of dynamical times, in view of the unphysical effects of particle discreteness and softening imposed by the numerical method. And of course at such densities, the ISM of real galaxies is much more volatile than the idealized compressible fluid model adopted in these calculations. Nonetheless, we might still want to know about the evolution of the *rest* of the system, including the dark matter, the collisionless stellar component, and the low-density gas.

To study the further evolution of the remnant from encounter A, we therefore took the configuration at $t = 3$ and converted the 11,119 gas particles within the central cloud to collisionless particles, while retaining the full hydrodynamical description of the 5265 gas particles elsewhere. The thermal energy of the converted gas particles

was added to their random motions. While this procedure might be said to mimic a sudden burst of star formation, it is probably best regarded as a simple trick for representing the gravitational effects of the high-density gas in the rest of the calculation. Adopting the latter point of view, we will exclude the converted gas particles when discussing the distribution of the luminous component.

We followed this system until time $t = 6$, with results summarized in Figure 11. At the end of this calculation, the stellar distribution in the body of the remnant is fairly relaxed, motivating the discussion of radial profiles in § 4.1. As one can see from the enlarged views in Figure 11, the main body of the stellar remnant is quite nearly oblate at small radii; the remnant's shape and kinematics are described in § 4.2. The tails themselves stretch to ever greater lengths, but eventually much of the gas and stars

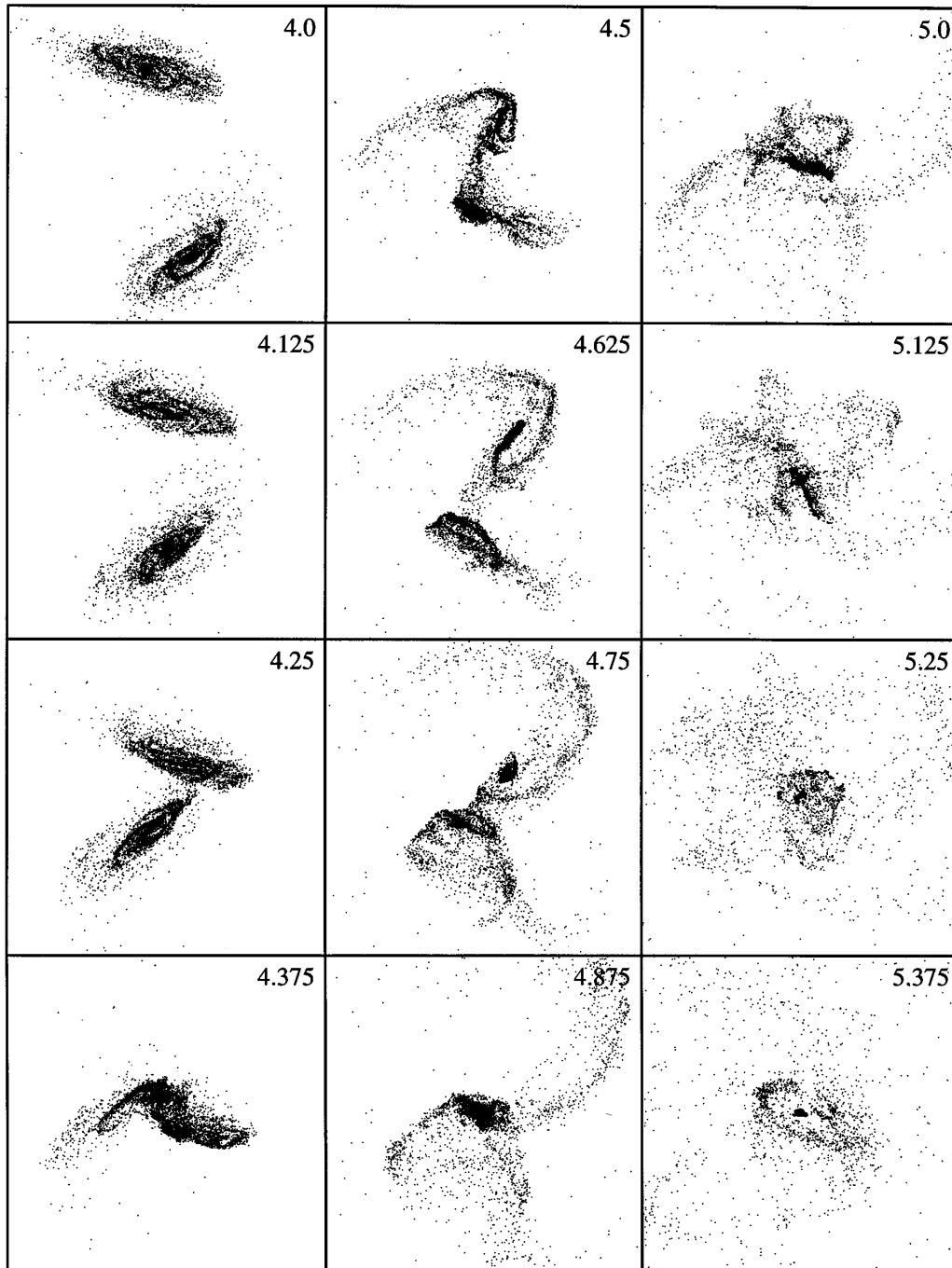


FIG. 10.—Evolution of the gas distribution during the final passages of encounter 4, projected onto the orbital plane. Frames before $t = 5$ have fields of 1.2×1.2 length units; later frames have fields of 1.0×1.0 , 0.8×0.8 , 0.6×0.6 , and 0.4×0.4 length units, respectively.

that comprise them will turn around and fall back into the remnant. The infalling stars oscillate back and forth through the potential, where they may form loops, plumes, or shells (Paper I; Hernquist & Spergel 1992; Hibbard & Mihos 1995), while the gas is shocked and dissipates its kinetic energy. This gas eventually settles into a warped disk as seen in the rightmost panels of Figure 11 and as further described in § 4.3. Also apparent in this figure is the tendency of the tails to break up into overdense clumps. This fragmentation process will be examined in § 4.4; here, we merely note that the object near the leftmost edge of the gas frames at $t = 6$ is one such clump that happens to be in a rather tightly bound orbit about the merger remnant.

In passing, it is amusing that the tails in the edge-on view at the bottom left of Figure 11 are reminiscent of those of “The Mice,” NGC 4676, as reconstructed by Toomre & Toomre (1972). This generic resemblance is not surprising; the two disks in our model A spin in roughly the same directions, relative to their orbit, as do the disks in The Mice (Stockton 1974). An obvious difference, of course, is that there are still *two* Mice, while the galaxies in Figure 11 merged long before the final time shown.

4.1. Density and Temperature Profiles

As in previous studies, the remnants in our simulations have stellar density profiles falling off smoothly with radius.

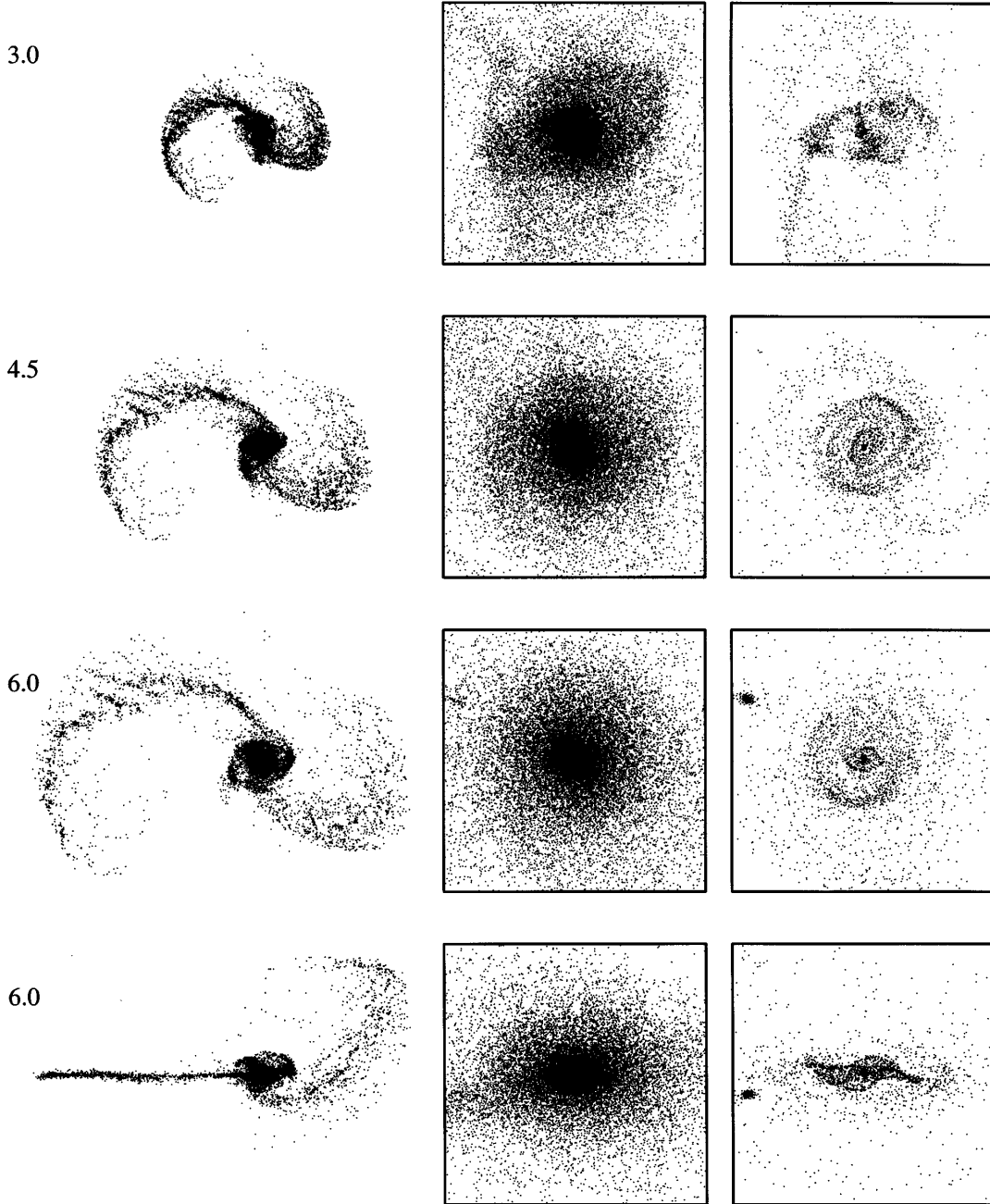


FIG. 11.—Continued evolution of the merger remnant produced by encounter A. On the left are views of the large-scale stellar distribution at the times indicated. The first three views are face-on to the orbital plane, while the last one is edge-on. In the middle are enlargements of the central stellar distribution; each frame is 0.8×0.8 length units. The frames on the right are similar but show the gas instead of the stars.

Figure 12a displays the spherically binned volume densities of the various collisionless components in encounter A at time $t = 6$. As one might expect, the inner parts of the remnant are dominated by stars from the bulges of the progenitors, while farther out, the luminous density is contributed mainly by disk stars, and at still larger radii, the dark halo is dominant. To parameterize these profiles, we fitted the density profile of each component separately using a simple analytic model which resembles a de Vaucouleurs (1948) $r^{1/4}$ law in projection:

$$\rho(r) = \frac{M}{2\pi} \frac{a}{r} \frac{1}{(r+a)^3}, \quad (4.1)$$

where a is a scale length and M is total mass (Hernquist 1990b). The appropriate value of M for each component is

simply the total mass bound to the remnant. We measured the half-mass radius $r_{1/2}$ of each component directly from the simulation and then set $a = (1 + \sqrt{2})^{-1} r_{1/2}$, as implied by equation (4.1). The results of this exercise are plotted in Figure 12b and summarized in Table 2.

Although the simulated profiles exhibit cores while the density profile above does not, the density of each separate component is elsewhere well fitted by equation (4.1) with the appropriate values of M and a from Table 2. In particular, the fits to the separate distributions of bulge, disk, and halo particles are excellent, which implies that each in projection closely resembles a de Vaucouleurs profile. Likewise, the bulge and disk together give a good de Vaucouleurs law in projection with a smooth transition between the components. These results are quite consistent with those

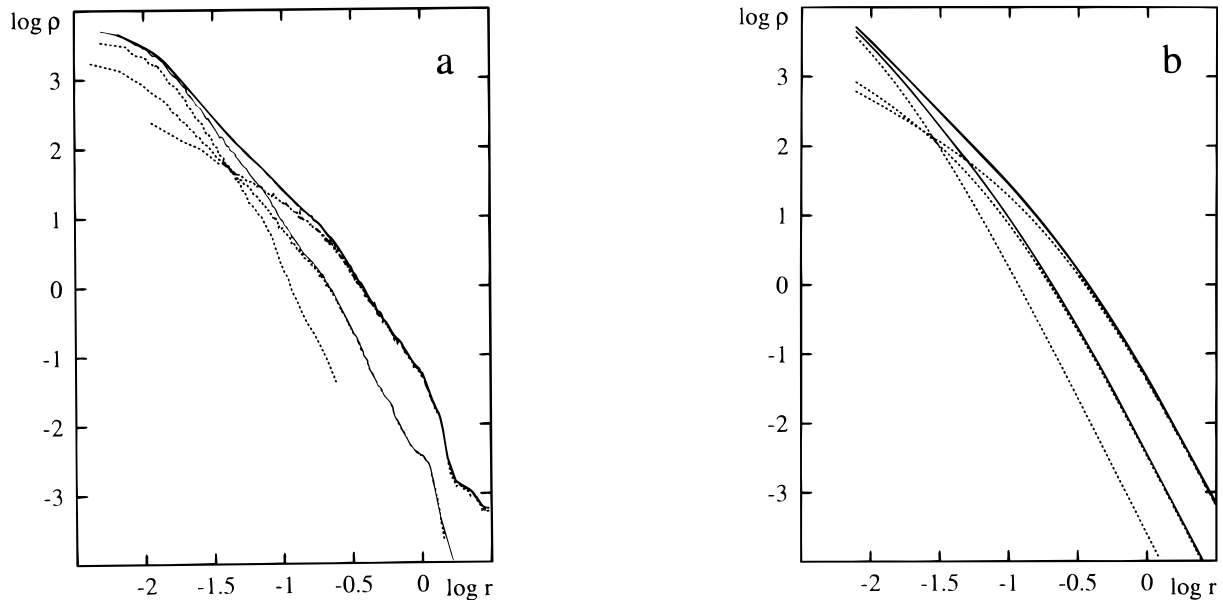


FIG. 12.—(a) Density profiles for the collisionless components of the remnant produced by encounter A. The heavy solid line shows the total density, while the lighter solid line shows the density of luminous material only. Dotted lines show, in order of increasing central density, the halo, disk, and bulge components, respectively. (b) Similar plot derived from fits to the individual components using eq. (4.1) and the parameters listed in Table 2.

obtained in earlier collisionless simulations (see, e.g., Paper I; Hernquist 1992, 1993a), which indicates that the gas has relatively little effect on the radial distribution of the collisionless matter.

The fate of gas in the merger remnant depends on its thermodynamics; if the gas cannot cool radiatively, its distribution resembles that of the stars. This is illustrated in the top panel of Figure 13, where we compare density profiles of the gas and disk stars in the remnant produced by encounter 1_A. Besides displaying as continuous lines the gas and stellar densities estimated by binning particles in spherical shells as above, we also show the densities computed at each gas particle's position using the SPH procedure. There is good agreement between the two estimates of the gas density, except in the outlying regions where spherical binning does not reflect the higher gas densities found in the tidal tails. The ratio of gas to stellar density is about 1:16 at the center and tapers to about 1:6 at $r \simeq 1$; thus, both components are effectively pressure supported, but the gas is slightly more extended. This may be due to a dynamical

effect noted by Navarro & White (1993); in simulations without radiative cooling, the gas is somewhat heated with respect to the collisionless material because the latter can interpenetrate while the gas cannot, which leads to an orbital phase difference that transfers kinetic energy to the gas. The temperature profile of the gas in encounter 1_A is represented in the bottom panel of Figure 13. Gas within the body of the remnant has been heated to a virial temperature of a few $\times 10^6$ K, while the small amount in the tidal tails has cooled below 10^4 K by adiabatic expansion.

In models in which the gas can dissipate, its final distribution is *very* different from that of the stars. Figure 14 portrays this in the remnant from encounter A at $t = 6$. Although the gas and disk stars had similar distributions in the progenitor galaxies, the gas is now much denser than the stars: nearly 60% lies in a region only ~ 0.0025 length units (~ 100 pc) in radius. The disk stars, on the other hand, have a half-mass radius $r_{1/2} \approx 0.16$ (~ 6 kpc). As discussed in § 3.2, this difference arises from the transfer of angular momentum from the gas to the surrounding collisionless matter. Depending on the effects of star formation, this finding has obvious significance for a variety of observed systems, including starbursts and possibly active galactic nuclei.

Figure 15 presents histograms of gas density at the end of simulations A, 1_I, and 1_A. The good agreement between encounter A and the isothermal version, encounter 1_I, is not terribly surprising since radiative cooling—as implemented here—keeps most of the gas near the cutoff temperature of 10^4 K (§ A3). Basically, these two calculations yield similar amounts of high-density gas; in encounter A, fully 66% of the gas has densities $\geq 10^4$, while in encounter 1_I, 57% has comparable densities, and another 9% of the gas has densities $\sim 10^3$. This material presumably had slightly different histories in these two simulations; in encounter A, it was incorporated into the dense inner blob, while in the isothermal case, it settled into a ring at slightly larger radii. In

TABLE 2
PARAMETER FITS TO REMNANT A

Component	$r_{1/2}$	M	Percentage Escaping
Bulge	0.032	0.125	0.0
Disk	0.162	0.324	4.0
Halo	0.503	1.859	7.1
Stars	0.112	0.449	2.9
Mass	0.399	2.308	6.3

NOTE.— M and $r_{1/2}$ are the mass and half-mass radius of each component, respectively; the last column gives the percentage escaping, which is not included in the fits. Here the “stars” are the bulge and disk, while the “mass” is all collisionless components.

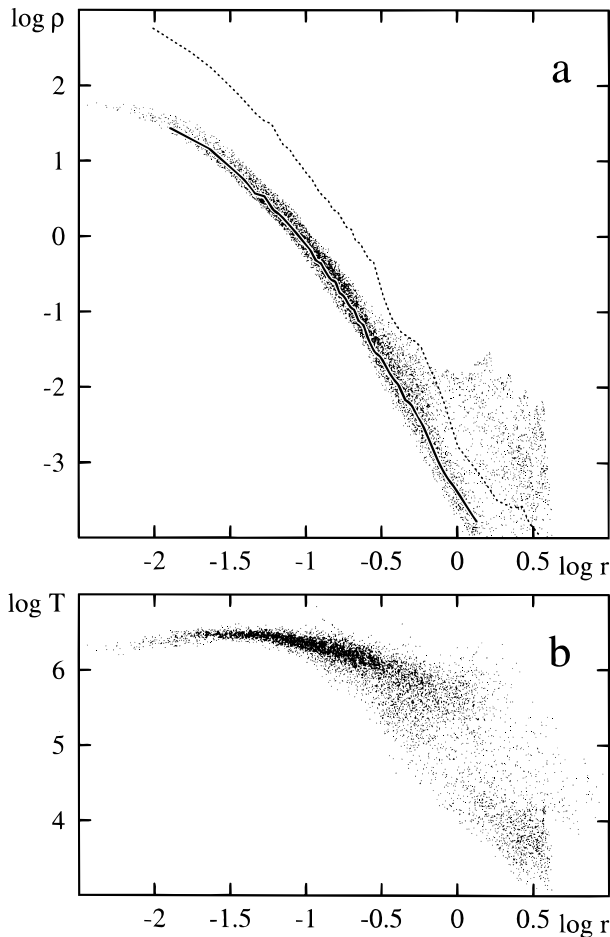


FIG. 13.—Density and temperature profiles for the remnant from encounter 1_A at time $t = 3$, plotted against radius. (a) Density of gas (solid curve and points) and disk stars (dotted curve). (b) Temperature of gas particles.

contrast to both of these simulations, the gas in encounter 1_A attains maximum densities of only $\sim 10^2$, as Figure 13 already reports.

4.2. Stellar Kinematics

On physical grounds, one might expect the concentration of gas toward the center of a merger remnant to deepen the

potential well and thereby increase the central density of the collisionless components as well. In fact, the effect of the gas on the radial distribution of the stars is not very dramatic; the central stellar density of remnant A is only about twice that of remnant A_0 . But the effects of the gas's gravitational field on the *kinematics* of the stellar component seem to be quite profound.

Figure 16 shows histograms of radial orbital periods for stellar particles in three closely related merger remnants; the solid, dashed, and dotted lines are from encounters A , A_0 , and A_1 , respectively. Stars with periods longer than the median have essentially identical distributions, within the uncertainties, in all three remnants. But for shorter radial periods, the three distributions are significantly different, with remnant A yielding the most short-period orbits, and remnant A_1 , the least. These differences arise because remnant A has a deeper potential well than remnant A_0 , which in turn has a deeper well than remnant A_1 .

We used the orbit classification technique of Paper I to examine the structure of these remnants. In this analysis, we “freeze” the potential at the end of the simulation and follow each particle for ~ 50 radial periods in this frozen potential, adopting a coordinate system (X , Y , Z) that diagonalizes the moment of inertia of the body of the remnant. If all three components of the particle's angular momentum vector change sign with time, the orbit is classified as a box. If the sign of the minor-axis (Z -axis) component of the angular momentum is preserved, while the other components change sign, the orbit is a Z -tube. Likewise, if the major-axis (X -axis) component is preserved, while the other components change sign, the orbit is an X -tube. Only $\sim 1\%$ of the bound orbits in these remnants do not fall into one of these three categories. However, this analysis does not distinguish between the two major families of X -tube orbits (de Zeeuw 1985a, 1985b), nor does it separate box orbits from boxlets (Miralda-Escudé & Schwarzschild 1989).

Our results are presented in Figure 17, where remnants A_1 , A_0 , and A are laid out from left to right in order of increasing potential well depth. The upper panels illustrate how luminous particles—from the bulges and disks of the original galaxies—are distributed among the different orbital families. Here, the highest curve in each panel shows the cumulative distribution of binding energy E for all lumi-

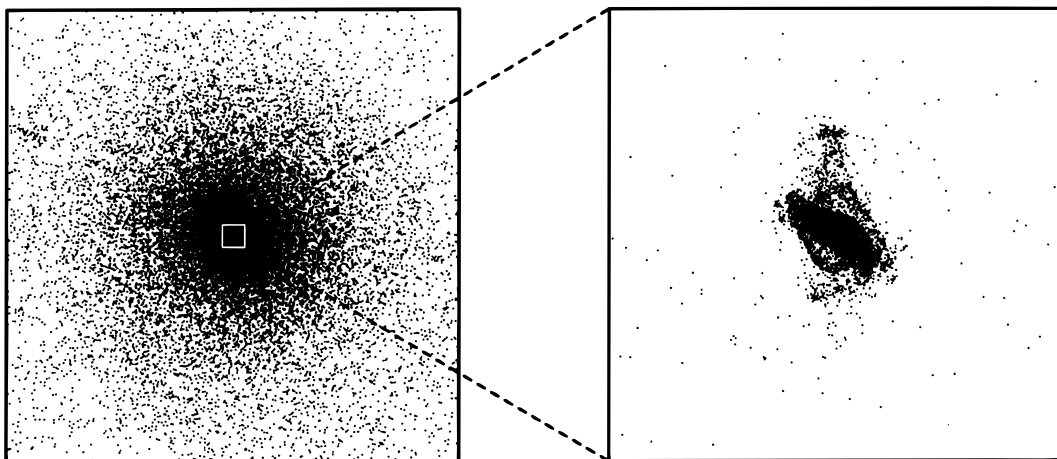


FIG. 14.—Views of stars (left) and gas (right) in the merger remnant produced by encounter A at time $t = 6$. The stellar view is 0.8×0.8 length units, while the view of the gas is enlarged by a factor of 20. Over 60% of all the gas in this remnant lies in this dense central blob.

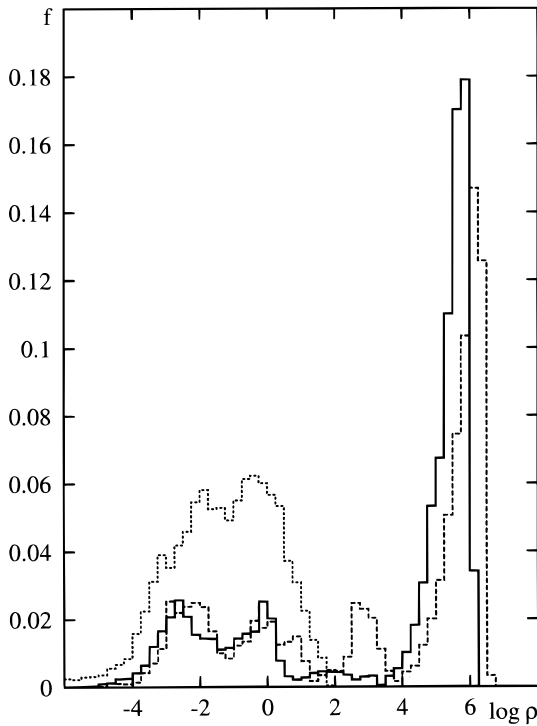


FIG. 15.—Histograms of gas density for the merger remnants from encounters A (solid line), 1_1 (dashed line), and 1_A (dotted line), obtained at time $t = 3$.

nous particles, and the vertical space between each subsequent pair of curves shows the fraction of Z-axis tubes, X-axis tubes, and boxes, respectively. The dotted curves represent orbital fractions for an isotropic sample with the same energy distribution as the luminous particles; these curves thus indicate the phase-space volume available to each orbital family. The lower panels are scatter plots of specific angular momentum j_z and binding energy E for luminous particles in Z-tube orbits.

Comparing these plots, it appears that the depth of the potential well is highly correlated with the stellar kinematics. Remnant A_1 is composed largely of box orbits, with

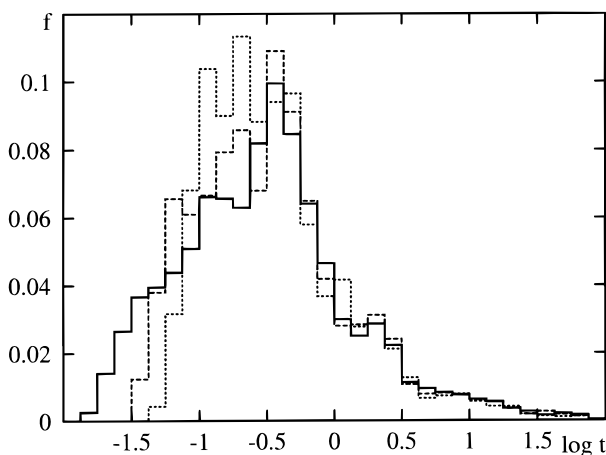


FIG. 16.—Histograms of orbital periods for luminous particles in the remnants produced by encounter A (solid line), encounter A_0 (dashed line), and encounter A_1 (dotted line).

some X-tubes. Indeed, this nearly prolate remnant, with axial ratios of 1:0.5:0.4, has a potential permitting almost no Z-tubes more tightly bound than the median. Z-tube orbits are prevalent only for the most loosely bound third of the luminous particles, and most of them circle the remnant in the same direction as the disks once spun and the galaxies once orbited one another. In contrast, remnant A has significantly fewer box and X-tube orbits and is largely dominated by Z-tube orbits. The oblate form of this remnant, with axial ratios of 1:0.9:0.6, generates a potential that can support Z-tube orbits of all energies, as indicated by the uppermost of the dotted lines. Tightly bound Z-tube orbits are evenly divided with respect to $j_z = 0$, while those more loosely bound follow the pattern in the other versions of this remnant. Remnant A_0 is intermediate between these two extremes; it has more Z-tubes and fewer boxes than remnant A_1 but does not exhibit the large population of tightly bound Z-tube orbits seen in remnant A.

Because only tube orbits maintain a definite sense of circulation about an axis, the angular momentum content of these remnants depends on the relative populations of the various orbit families. For example, remnant A, which has a large population of tightly bound Z-tube orbits, could in principle exhibit rapid rotation in its central regions. But as the lower right panel of Figure 17 shows, Z-tube orbits in the most tightly bound quartile of luminous particles are symmetrically distributed with respect to the $j_z = 0$ axis; the net streaming motion of this quartile is only $\sim 1\%$ of its velocity dispersion. Indeed, the angular momenta in the most tightly bound quartiles of remnants A and A_0 are so small as to be all but unmeasurable. Within the second most tightly bound quartile, the net streaming motions are an order of magnitude larger, and some meaningful comparisons can be made. In this energy range, remnant A rotates almost twice as fast as its dissipationless counterparts; moreover, the kinematic misalignment between the spin axis and minor axis of this gas-rich merger is only 11° , as compared to 25° and 18° for remnants A_0 and A_1 , respectively.

4.3. Gas Distribution and Kinematics

That gas which does not collect at the very center may contribute to the structure of a remnant by settling into a disk at larger radii. An example is seen in the lower right-hand panels of Figure 11, which show the distribution of gas in the continuation of encounter A. As loosely bound gas falls into the inner parts of the remnant, it shocks on encountering more tightly bound gas and dissipates its kinetic energy. By time $t = 4.5$, the infalling gas has formed a warped disk surrounding the central dense blob, and by $t = 6$, the disk has grown to a radius of ~ 0.4 length units (~ 16 kpc). The mass of this disk is ~ 0.005 mass units ($\sim 1 \times 10^9 M_\odot$), or roughly 20% of the initial gas mass of this system.

In Figure 18 this disk is viewed in projection along the minor axis of the merger remnant. Gas particles lying close to the principal plane are plotted as points, while those significantly above or below the plane are plotted as crosses or circles, respectively. The leading spiral pattern that emerges is expected in a disk embedded in an oblate potential; the line of nodes rotates in the retrograde direction as orbits precess, and the closer to the center, the shorter the precession period. Beyond a radius of 0.4 length units, the gas distribution becomes more irregular and cannot prop-

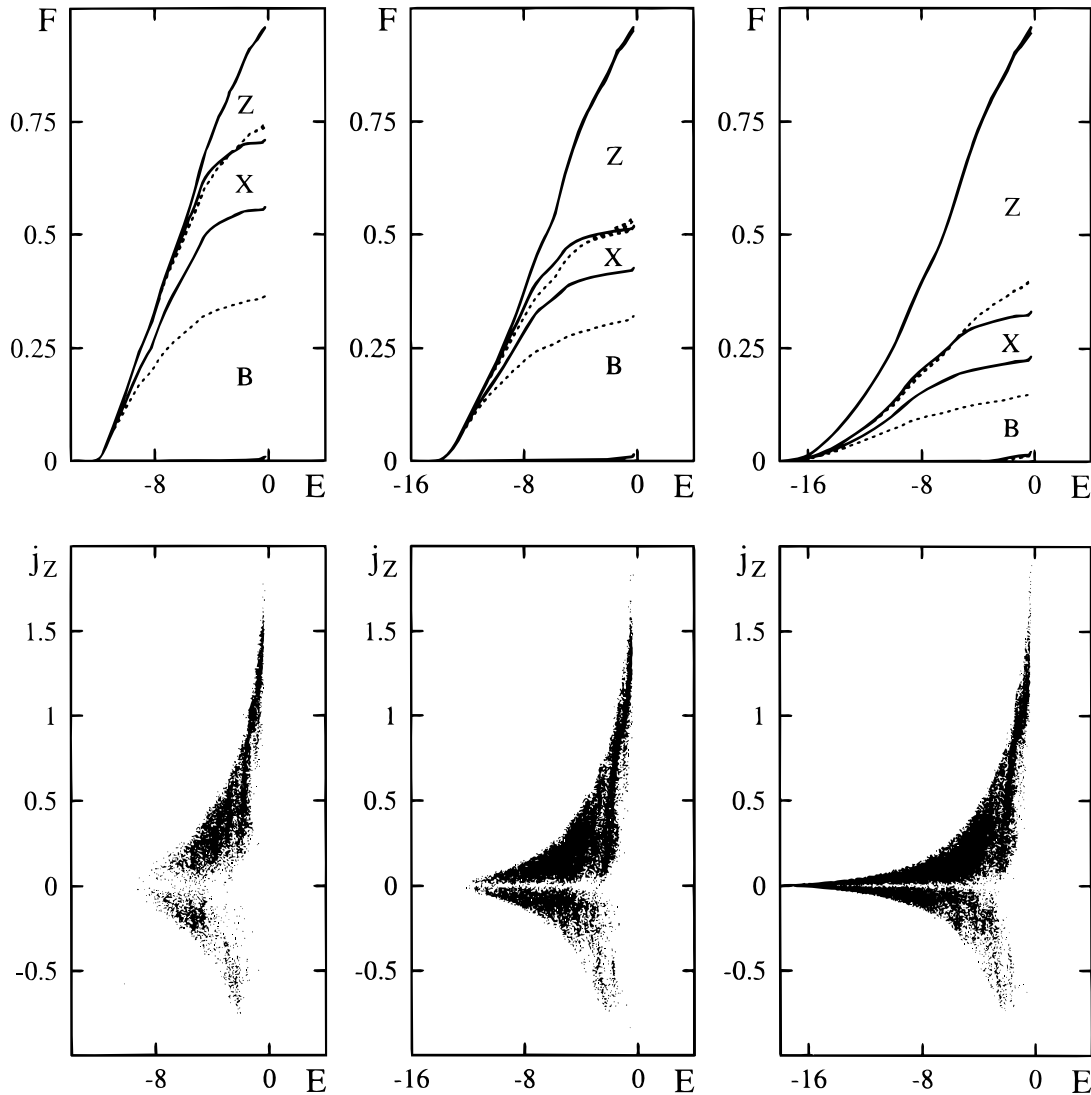


FIG. 17.—Orbit structure of merger remnants A_1 (left), A_0 (middle), and A (right). The top panels show how the populations of different orbital families depend on binding energy; here the regions labeled “Z,” “X,” and “B” represent the cumulative fractions of Z-tubes, X-tubes, and boxes, respectively. Solid lines show results for all luminous particles, while dotted lines show results for an isotropic distribution (see text). The bottom panels show specific angular momenta of particles in Z-tube orbits.

erly be called disklike; nonetheless, in angular momentum space the warped gas disk appears to join smoothly onto the gas falling in from the tidal tails. The largest contribution appears to come from the tail associated with the inclined galaxy, perhaps because this tail was not launched out so far and consequently has fallen back faster.

This disk is reminiscent of the warped dust disk in the early-type galaxy NGC 4753 (Steiman-Cameron, Kormendy, & Durisen 1992), although its tilt is more extreme: as much as 40° , as compared to $\sim 15^\circ$ for NGC 4753. Steiman-Cameron et al. attribute the disk in NGC 4753 to the accretion of a gas-rich satellite galaxy on an inclined orbit. In the remnant described here, the disk forms by continued accretion of misaligned gas from the tidal tails. It is possible that some warped disks in early-type galaxies may have formed not by accretion of low-mass companions but rather as a by-product of mergers between comparable progenitors. A galaxy worth mentioning in this context is NGC 5128, also known as Centarus A (van Gorkom et al. 1990; Nicholson, Bland-Hawthorn, & Taylor 1992;

Schiminovich et al. 1994); although its warped disk is generally blamed on the accretion of a small companion, the rather disturbed structure revealed at the lowest light levels may imply that this system had a rather more violent origin (see, e.g., Schweizer 1986).

Encounter 4 produces a remnant with even more distinctive gas kinematics: a nested pair of *counterrotating* disks (Hernquist & Barnes 1991). At the time $t = 6$ shown in Figure 19, the outer disk, while rather diffuse, can be traced out to a diameter of ~ 0.2 length units; edge-on, it is only 0.01 units thick and exhibits a modest integral-sign warp. In the lower panel of Figure 19, which shows velocities seen by an observer viewing the disks edge-on, the outer disk and gas at larger radii together trace out a nearly flat rotation curve with a peak-to-peak amplitude of ~ 4 velocity units. The inner disk, which appears “burned out” in the upper panel, is an oval ring with dimensions of 0.023×0.015 length units; edge-on, it is just 0.002 units thick. This component produces the narrow line slanting almost vertically across the lower panel of Figure 19, with a amplitude just

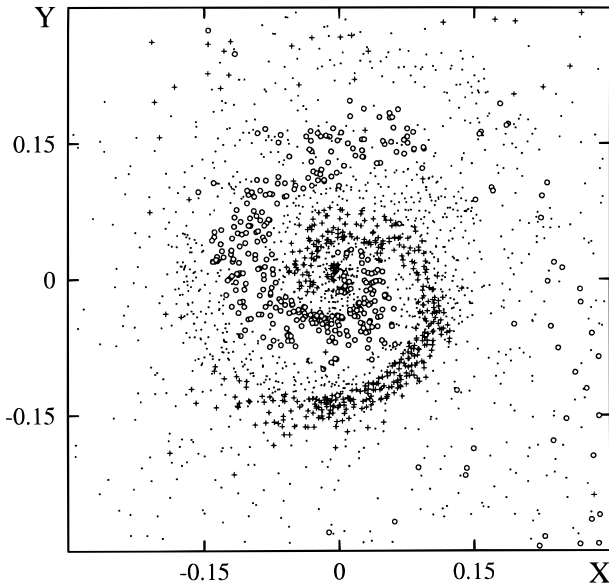


FIG. 18.—Face-on view of the warped gas disk in merger remnant A. Particles significantly above or below the disk plane are plotted as crosses or circles, respectively.

half that of its outer partner. At the instant shown here, the two disks are nearly counterrotating, with spin axes separated by 165° .

This remarkable state of affairs arises from the violent interactions chronicled in Figure 10, but since intermediate time frames are not available for this simulation, it is difficult to follow the actual formation process. The counter-rotating inner disk appears to be in place by time $t = 5.25$, while the outer disk can be seen in the last frame of Figure 10. Comprising $\sim 60\%$ of all the gas in the system, the inner disk is largely composed of gas that flowed to the centers of the individual galaxies between their second and third passages. The outer disk, which at time $t = 6$ comprises $\sim 20\%$ of the gas, comes from material initially at somewhat greater radii. Because the outer disk has not suffered so much inflow, it more or less shares the angular momentum distribution of this remnant's body. The inner material, on the other hand, has lost a great deal of angular momentum. One might expect that what angular momentum the inner disk gas retains might not be well correlated with its initial angular momentum, but it is still surprising to find it actually rotating in the other direction!

Curious to see how this system might evolve, we extended this calculation to $t = 8$ time units, with somewhat puzzling results: The inner disk loses its angular momentum and collapses to an unresolved blob by $t = 8$. As there is little evidence for direct hydrodynamic interaction of the two disks, gravitational interaction is a prime suspect, but at present we do not understand how this happens or to what extent the force softening used in the gravitational force calculation may have suppressed even more violent instabilities.

One more curiosity concerning this simulation is that its purely stellar cousins, encounters B and 6 of Paper I, both produce remnants exhibiting intrinsic twists, rather complex figure rotation, and dramatic kinematic misalignments, *including* evident intermediate-axis rotation. Indeed, it was by no means clear that either remnant had really approximated an equilibrium by the end of the simulations.

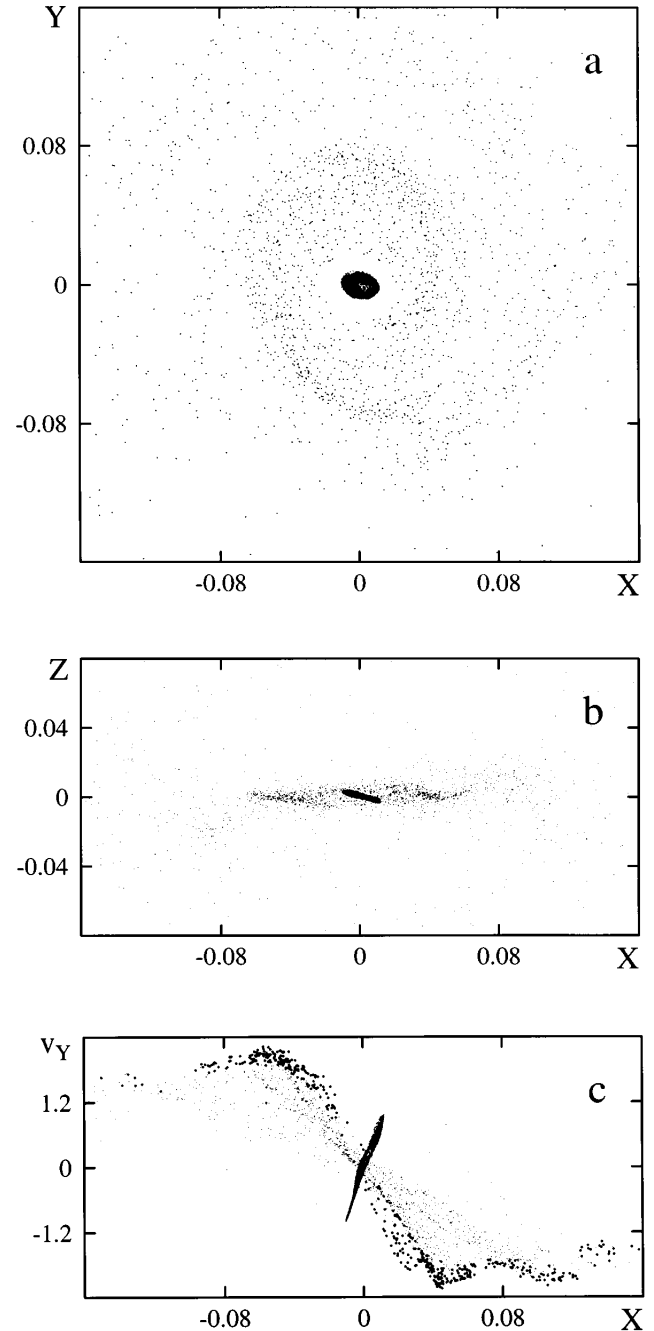


FIG. 19.—Counter-rotating gas disks in the remnant produced by encounter 4. (a) Face-on projection of the gas disks; the solid oval at the center is the inner disk, while the loosely defined spiral pattern belongs to the outer disk. (b) Edge-on view of the two disks. (c) Line-of-sight velocities seen from the edge-on projection; the counter-rotating inner disk produces the dark streak rising to the right across the middle of the plot. Points in the outer disk within 0.025 length units of the Y-axis are plotted as small filled circles to highlight the shape of the rotation curve.

4.4. Bound Structures in Tidal Tails

That tidal tails can fragment after formation should not be surprising; although large-scale tidal forces lead to complex global motions, locally the material in tails is a freely expanding distribution of stars and gas and, as such, may develop gravitational instabilities. Gerola, Carnevali, & Salpeter (1983) illustrated the formation of bound objects

in an expanding distribution of collisionless particles, while Barnes & Hernquist (1992) and Elmegreen, Kaufman, & Thomasson (1993) specifically discussed formation of dwarf galaxies in tidal tails. Like its collisionless counterparts (see, § 4 and Fig. 10 of Paper I), encounter A forms a number of bound structures in its tidal tails.

Section 5 of the videotape shows the formation of the most massive bound object in the tidal tails of encounter A. This clump might indeed qualify as a dwarf galaxy; it has a mass of ~ 0.002 ($\sim 4 \times 10^8 M_\odot$), half of which is contained in a radius of ~ 0.02 (~ 800 pc). In this animation sequence, blue and green represent the stellar and gaseous particles, respectively, which fall within a radius of 0.04 length units of the “dwarf” at time $t = 3$, while other luminous particles belonging to the two galaxies are shown in red. The video follows the dwarf as it evolves by centering each frame on the center of mass of the blue particles.

The animation starts with a view of the direct disk at time $t = 0.5$. Initially, both constituents of the “dwarf-to-be” describe leading spiral patterns, but the gas comes from an extremely drawn-out filament, while the stellar component is a good deal more localized. Before the passage at $t = 1$, the stellar component is first drawn together and then stretched by differential rotation of its parent disk; it appears that the stellar component of the massive dwarf was formed from a fragment of trailing spiral structure. The interaction between the galaxies launches this material away as part of the tail, and once removed from the tidal field of its parent, the stellar component gently collapses. The gaseous component, in contrast, remains extended until convergent flows drive the gas into a thin “ridge line” along the tail; the gas so gathered gives the dwarf a remarkably high gas fraction of $\sim 25\%$, as compared to 10% for the disk it formed from. Subsequently, the gas relaxes to a distribution significantly more concentrated than that of the stars. This state of affairs is similar to the evolution that may be responsible for producing “spokes” in ring galaxies (see, e.g., Hernquist & Weil 1993).

Barnes & Hernquist (1992) used a percolation algorithm to identify more than 20 bound clumps in the tidal tails of encounter A. These range from the massive dwarf just described to loosely bound configurations $\lesssim 10\%$ as massive. The distribution of these objects at time $t = 3$ is shown in Figure 20a; clump members are plotted as small filled dots, while the circular inset shows the gaseous and stellar particles in the vicinity of the massive dwarf. It is noteworthy that *most* of these bound objects are scattered along the outer curve of the tail from the direct disk. There are a number of reasons why this region might yield many bound objects—the velocity dispersion is relatively low in the outer part of the pre-encounter disk, the outward motion of this tail quickly removes collapsing structures from the tidal field of the primaries, and the simple geometry of this direct passage seems to introduce less random motion than do more inclined passages.

Figure 20b shows bound clumps identified in the same way at time $t = 6$ (note the change of scale to allow for the expanded tails). Many of the particles in these clumps were also in clumps at $t = 3$, although some have diffused in or out of loosely bound objects due to discreteness effects. Thus, the structures formed in these tidal tails generally persist until tidally disrupted. One such case is the massive dwarf, which was partly disrupted by tidal forces during its first orbit about the body of the merger remnant. The inset

in Figure 20b shows that the *stellar* component of this object, which was never very tightly bound, has been largely stripped by tidal forces, populating the loop extending toward 4 o'clock with respect to the center of the remnant. The gaseous component, which is more compact, better resists tidal disruption and is seen at approximately 10 o'clock; its future orbit roughly tracks the loop of stellar material. Meanwhile, the return of material from the tidal tails has carried two more small clumps in toward the remnant, where they are likely to be disrupted. Note, however, that many of the objects in the outer tails have *extremely* long orbital periods and so are safe from tidal disruption by the merger remnant.

The relatively slow evolution of the structures in these tails between times $t = 3$ and 6 is natural given that the tails, considered in isolation, are highly unbound—thus, structure “freezes out” much as it does in a universe with $\Omega \ll 1$. It follows that most of the bound objects which form in tails do so very shortly after the tails themselves are released, while the stellar density is still a fair fraction of the “critical density.” This prediction is supported by reviewing the trajectories of those disk particles that end up in bound objects. In this respect, the rather early and gentle collapse of the *stellar* distribution depicted in section 5 of the videotape is actually typical of the other bound objects; most, indeed, were quite well localized at first passage.

Further evidence for the role of stellar density fluctuations in forming these bound objects is provided by examining encounter A₀. Most of the individual objects seen in encounter A are also present in its collisionless analog. This result may seem less surprising when one notes that encounters A and A₀ also exhibit nearly identical spiral structures before their first passage. Such close correspondence supports the view that the tail structures in both simulations grew from the *same* set of Monte Carlo fluctuations in their common initial conditions and that dissipative effects are not crucial in forming such structures. In this respect, the massive dwarf depicted in section 5 of the videotape may not be so typical; encounter A₀ does not produce an analogous object. A careful examination of this simulation shows that the stellar component does become localized much as in encounter A but does not attain the density contrast needed to remain bound in the tidal field of the primary galaxies. As noted in § 3, the gas content of the disks in encounter A increases the amplitude of the stellar spirals by lowering the overall Q value. Moreover, the gas significantly increases the tidal stability of the massive dwarf. Thus, the fact that no analog of this object survives in encounter A₀ is not too surprising and does not conflict with the hypothesis that the proximate origin of the bound structures in these simulated tails is the collapse of stellar overdensities.

5. DISCUSSION

5.1. Relation to Earlier Work

In many respects, the simulations reported here are directly descended from the ground-breaking calculations of Negroponte & White (1983). Like these authors, we focus on encounters of equal-mass gas-rich disk galaxies stabilized by dark halos, and like them, we find that such encounters lead to rapid mergers, with about half of the gas collecting within the unresolved core of the resulting merger remnants. Our simulations differ from those of Negroponte & White in that we employ more extensive dark halos and

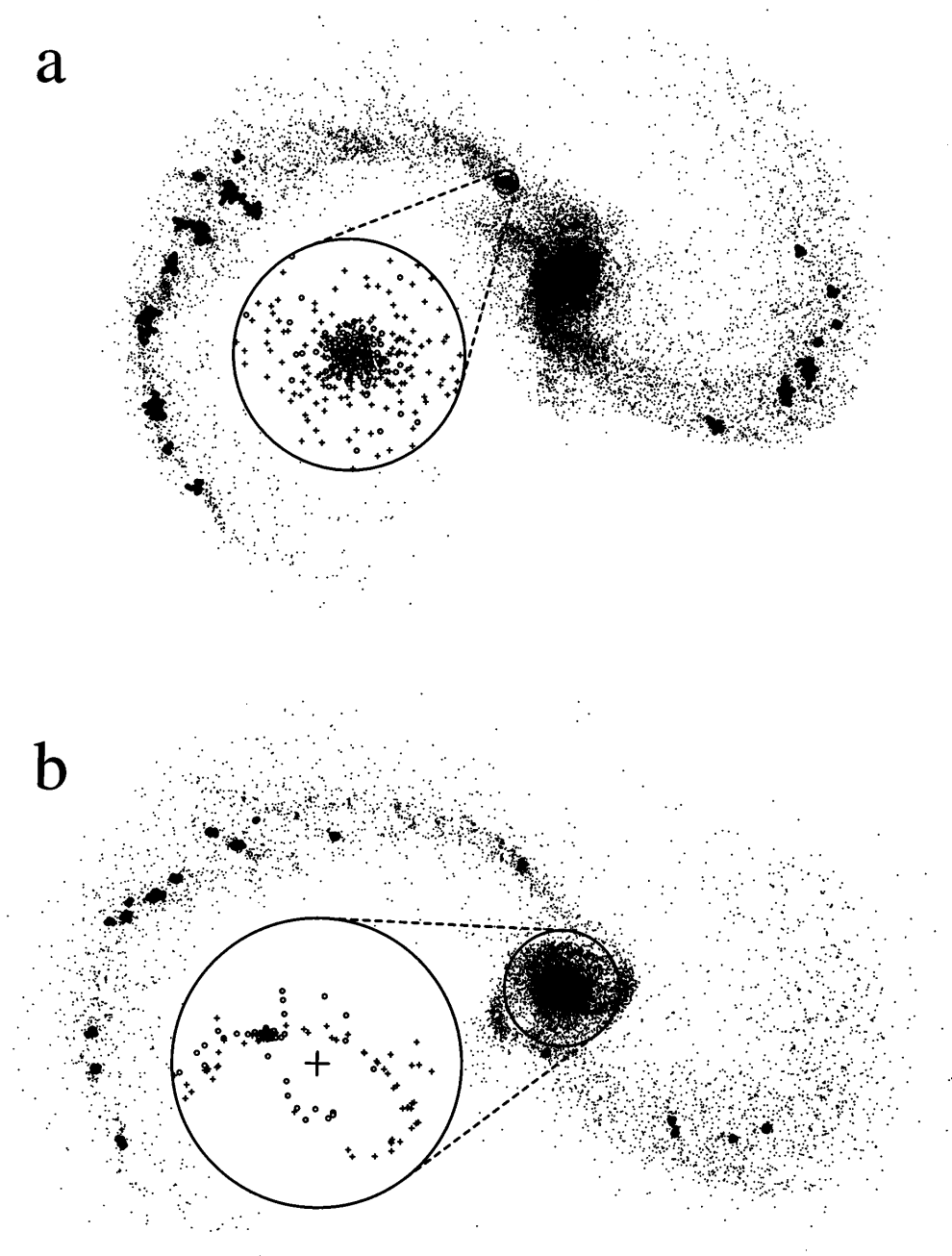


FIG. 20.—Bound structures in the tails of encounter A. (a) Small filled circles show bodies in bound structures at time $t = 3$. The circular inset shows the most massive such object; plus signs show the stellar distribution, while small open circles represent the gas. (b) As above, but at time $t = 6$. The scale has been shrunk by a factor of 2. The circular inset shows the present distribution of stellar and gaseous particles identified as belonging to the massive object at time $t = 3$, while the large plus sign marks the center of the merger remnant.

nearly 10^2 more particles; moreover, we treat the ISM as a compressible gas that can cool radiatively, instead of a granular medium composed of sticky particles undergoing physical collisions. Nevertheless, the basic agreement between our results and theirs suggests that the dynamics responsible for the gas inflows is relatively insensitive to the detailed representation of the interstellar material.

The dynamics of inflows was partly elucidated by Noguchi (1987, 1988), who showed that self-gravitating stellar disks may develop bars in response to strong tidal perturbations and that gas in such barred potentials tended to collect at the centers of the disks, much as in earlier simulations of gas flows in barred disk galaxies (Schwarz 1984). Similar calculations led Combes et al. (1990) to argue that *gravitational* torques are responsible for driving the gas

inward. These calculations employed two-dimensional disks and rigid halo potentials and thus could not model the rapid orbital decays expected in the close, relatively slow encounters that apparently lead to the most luminous starburst galaxies. The logical connection between these experiments and those of Negroponte & White was explicitly demonstrated by BH91, who described one of the present simulations and measured the gravitational torque exerted by a barred disk in a completely self-consistent calculation.

Our results can also be compared to the simulations in Paper I, since the same encounter parameters were used in both studies. On the one hand, gas evidently has little effect on the global evolution of a merger. Orbit decay appears to be slightly accelerated when gas is included, but this effect is

weak and not out of proportion to the relatively small gas content of our model disks. On the other hand, the structure of the resulting merger *remnants* can be *drastically* altered by modest amounts of gas. In particular, the remnants examined here tend to be rounder than those in Paper I, and they may exhibit better alignment between their spin and minor axes. As described in § 4, the degree to which the spin and minor axes are aligned is a direct consequence of the orbits populated by the merger. Clearly, the distribution of orbit families is strongly affected by the presence or absence of gas in the models. Similar findings have been reported in models of galaxy formation by gravitational collapse (see, e.g., Katz 1991, 1992; Katz & Gunn 1991; Udry 1993; Dubinski 1994).

5.2. Relation to Observations

Since the work of Larson & Tinsley (1978), it has been widely recognized that interacting galaxies undergo bursts of star formation. Moreover, systems chosen on the basis of their high infrared luminosities often have tails and other tidal features characteristic of mergers between gas-rich spiral galaxies (see, e.g., Soifer et al. 1984a, 1984b; Allen, Roche, & Norris 1985; Joseph & Wright 1985; Sanders et al. 1986; Armus, Heckman, & Miley 1987; Sanders et al. 1988a, 1988b; Kleinmann et al. 1988; Sanders 1992). Observations at millimeter wavelengths have shown that these objects have dense central clouds of molecular gas with masses comparable to the total gas content of large gas-rich disk galaxies (see, e.g., Young et al. 1984, 1986; Sanders & Mirabel 1985; Sanders et al. 1987). In many cases, more than half of the gas is concentrated within the inner kiloparsec of the system (see, e.g., Scoville et al. 1986; Sargent et al. 1987; Sargent, Sanders, & Phillips 1989; Sanders, Scoville, & Soifer 1991; Tinney et al. 1990; Scoville et al. 1991). Arp 220, for example, has an infrared luminosity $1.5 \times 10^{12} L_{\odot}$ and possesses a nuclear concentration of gas a few hundred parsecs in radius containing of order $2 \times 10^{10} M_{\odot}$ of molecular material (see, e.g., Scoville 1992, but also Shier, Rieke, & Rieke 1994 for some cautionary remarks about the inferred amounts of molecular gas).

Like several previous experiments, our models show that central gas concentrations like those found in the ultraluminous infrared galaxies arise naturally as the result of the dynamics of violent mergers. In particular, the quantities of gas involved and the timescales over which they accumulate are consistent with the observations. The exact relationship between the gas concentrations arising in the models and the bursts of star formation that presumably ensue is problematic, although simulations incorporating empirical—and largely ad hoc—rules for converting gas to stars yield star formation rates comparable to those observed in ULIR starburst galaxies (see, e.g., Mihos & Hernquist 1994b, 1996).

Galactic collisions like those studied here can also account for some of the properties of elliptical galaxies, strengthening the interpretation that many ellipticals originate from mergers of disk progenitors. While our sample of models is not large, they demonstrate that systems with shapes and luminosity profiles similar to those of ellipticals can be formed by this process (see also Heyl, Hernquist, & Spergel 1994). Moreover, the central inflows of gas provide a mechanism for circumventing phase-space constraints that pose serious difficulties for the formation of elliptical

galaxies by mergers of purely *stellar* disks (see, e.g., Carlberg 1986; Lake 1989; Vedel & Sommer-Larsen 1990; Hernquist, Spergel, & Heyl 1993).

The simulations presented here reaffirm that gas inflows can produce subsystems with kinematics similar to those of the gas disks observed in some merger candidates (Schweizer 1982, 1986). Following Schweizer (1990), we conjecture that star formation from such disks may yield stellar components like the counterrotating cores found in many normal ellipticals (Kormendy 1984; Franx & Illingworth 1988; Jedrzejewski & Schechter 1988; Bender 1990a). In contrast to the suggestion that counterrotating structures develop as the result of satellite accretion (Kormendy 1984; Balcells & Quinn 1990), this dissipative formation mechanism predicts that decoupled cores are dynamically cold, as line profile observations often seem to indicate (Bender 1990b; Rix & White 1992; Forbes, Franx, & Illingworth 1995).

Our calculations also show that the return of gravitationally bound material from the tidal tails of merging galaxies can yield fine structures like those seen in some elliptical galaxies (Seitzer & Schweizer 1990). Stellar tails that are accreted by the remnant may form loops, shells, and “X-structures” similar to those seen when large galaxies accrete low-mass companions (see, e.g., Quinn 1984). Likewise, infalling gas from the tails may form warped disks similar to the one in the dusty S0 galaxy NGC 4753 (Steiman-Cameron et al. 1992). Shells and warped gas disks are certainly not proof that a merger has taken place, but when other signs of a major merger exist, there is no need to invoke additional accretion events to explain such features.

As described in § 4, tidal tails may fragment under their own self-gravity. Observations from Zwicky (1956) onward show that the tails of a number of merger candidates are not smooth but rather contain distinct overdense regions or knots (Schweizer 1978; Mirabel, Lutz, & Maza 1991; Colina, Lipari, & Macchetto 1991). These knots often appear to be sites of ongoing star formation (see, e.g., Mirabel, Dottori, & Lutz 1992; Hibbard et al. 1994), and many appear sufficiently well defined to survive as dwarf galaxies. Recently, Elmegreen et al. (1993) have described observations of incipient knots in tidally interacting disk galaxies; this suggests that gravitational collapse begins as soon as tail material is extracted from the shear flow of its parent disk. At present, structural details are known for only a few prominent knots in the tails of well-studied systems. The diffuse “dwarf” in the southwest tail of NGC 4038/9 (Mirabel et al. 1992), and the two rather more conspicuous objects in the tails of NGC 7252 (Hibbard et al. 1994), all appear to be gas-rich systems. Dynamical mass estimates hint that these objects do not contain much dark matter, in accord with the simulation results, but in contrast to most of the dwarf galaxies in the vicinity of the Milky Way (see, e.g., Kormendy 1987a; Pryor 1992). In other respects the sizes, luminous masses, and gas fractions of these tail fragments appear consistent with the rather broad range of parameters characterizing dwarf irregular and elliptical galaxies (see, e.g., Mould 1992).

5.3. Outstanding Issues

5.3.1. Physics of Inflows

In these and other simulations, inflows are observed when the angular momentum of the gas is removed from it

by the collisionless disk material via gravitational torques. These torques arise because the stars and gas in a disk respond differently to tidal forces. The question then arises as to why this difference exists.

The inflows in our models occur when the galaxies are severely distorted and the gravitational potential is changing rapidly with time. In a rapidly varying potential, the gas will be unable to locate closed orbits since such families of orbits change on a dynamical timescale. Therefore, gas streams are likely to intersect and form shocks, converting kinetic energy into heat and thence to radiation, presuming that the gas can cool. Since the stars are collisionless, they are not subject to similar constraints on their motions, and it *must* be the case that the gas and stars will respond differently. It seems clear that the gas loses energy monotonically during this evolution, but it is less obvious that the differences between the two components must always conspire so as to transfer angular momentum from the gas to the stars.

While angular momentum transport in *barred* disks has been studied in detail by a number of workers (see, e.g., Athanassoula 1992), the inflow phenomenon seems more general. For example, Hernquist (1989a, 1989b) and Hernquist & Mihos (1995) report inflows in disk-satellite mergers even though bars did not develop in these encounters. The final coalescence of the rotating gas rings seen in section 4 of the videotape provides another example; hydrodynamic interactions with the surrounding gas are not important, so the forces responsible for the remarkably small angular momentum of the final gas cloud are presumably gravitational, but the details are hard to establish. Experiments that abstract the crucial features of gas flows from the rather messy models we have analyzed here might provide a more promising framework for examining this issue.

Entropy considerations suggest a partial explanation of the inflows observed in these and other simulations. The entropy of the radiation emitted when shocked gas cools presumably exceeds the negentropy of the gas as it becomes concentrated toward the center of the remnant. Consequently, a merger remnant evolves toward higher entropy by losing energy to radiative cooling. Analogous behavior occurs in other kinds of systems: Stars evolve toward higher entropy by emitting radiation, while star clusters become more centrally concentrated as they undergo core collapse. The exact rate of energy loss depends on the physical circumstances; in an isolated disk, angular momentum constrains the inflow of gas to a viscous timescale, but this barrier is breached in the time-dependent nonaxisymmetric potential of a pair of merging galaxies. Thus, while evolution toward higher entropy may explain why gas collects at the centers of merger remnants, this argument does not directly account for the remarkable *efficiency* of this process.

In passing, it seems appropriate to discuss here some numerical uncertainties that might affect the inflows in the simulations. Hernquist (1993b) has shown that the use of variable smoothing lengths in the TREESPH code may cause energy conservation errors of $\sim 10\%$ if the thermodynamic evolution of the gas is calculated by integrating its specific entropy and that comparable errors in entropy presumably occur when the internal energy of the gas is integrated instead (e.g., § A2). Such errors are disconcerting, but it seems unlikely that they have a large effect the evolution of the gas since its thermal history is so heavily dominated

by radiative cooling. Nelson & Papaloizou (1994) have shown that these errors can be controlled by deriving the SPH equations of motion from a Hamiltonian that explicitly includes variable smoothing; this refinement seems worth including in future calculations.

5.3.2. ISM Physics

Looking beyond the idealized dynamics of the models, it should be noted that detailed behavior of inflows in real galaxies may not resemble that seen in our simulations. The limited dynamic range of our models represents galactic gas in a very simplified manner, glossing over the complex structure of the ISM (see, e.g., McKee & Ostriker 1977). It is encouraging that the main results presented here are not very sensitive to changes in the artificial viscosity or the model equation of state, provided that the gas is allowed to radiate the heat imparted in shocks. Indeed, similar results have been obtained with sticky-particle codes which employ a discrete-cloud model for the interstellar gas, notwithstanding that ours is, in spirit, a true continuum representation. A weakness of our approach is that multiphase gas flows should interpenetrate to some extent; thus, where our simulations show a narrow shock front, the gas in real galaxies will show broader and more complex structures. Clearly, this consideration *must* be important on small scales but is probably less critical on the kiloparsec scales modeled most accurately in our calculations, since even a lumpy medium may be described as a continuum fluid on scales much larger than the mean free path of individual clouds. In principle, this limitation could be overcome with an increase in computing power of roughly 10^4 , which would make possible SPH simulations a multiphase ISM on the scale of entire galaxies (Barnes & Hernquist 1993).

Effects related to star formation are more problematic. In particular, feedback can modify gas flows, especially in dense regions, by the input of heat and kinetic energy into the medium. Preliminary results by Mihos & Hernquist (1994a, 1994b, 1994c, 1996) indicate that feedback does not inhibit the gas inflows seen in the simulations and that gas consumption does not prevent intense starbursts from developing, although none of the models have yielded outflows like the “superwinds” observed in some infrared-luminous galaxies (see, e.g., Baan, Haschick, & Henkel 1989; Heckman, Armus, & Miley 1990). In any event, simple empirical rules for incorporating star formation and its effect on nearby gas cannot encompass all of the relevant physics, given our uncertainties concerning the IMF, which affects the supernova rate, and the detailed structure of the gas, which affects how much momentum it receives from supernovae. Progress on these fronts is not very likely until star formation itself is better understood.

5.3.3. Timing of Starbursts

An important observational question that may be illuminated by our models concerns the phase of an interaction when most starbursts are expected to occur. Prompt inflows may trigger bursts well before a full merger, while otherwise significant gas densities may be attained only as the galaxies merge. Observations suggest that the most intense starbursts occur during the period when the galaxies finally coalesce, rather than when they are well separated (see, e.g., Sanders 1992).

The models described above indicate that the timing of an interaction-induced starburst depends on the relative

orientations of the two disks *and* on the pericentric separation at first close approach. Although we have not included star formation in the models, it is clear from Figure 6 that the starburst history will be affected by changes in these parameters. Close, nearly direct encounters trigger rapid inflows, while wider and/or highly inclined passages do not. We have not completely isolated the dynamics responsible for the inflows, but it is evident that strong non-axisymmetric forces are essential. Invariably, stronger tidal responses in disks are associated with closer passages or direct collisions than wider or retrograde encounters.

This analysis is complicated by the fact that the response of a galaxy to a tidal perturbation depends also on its internal structure. Mihos & Hernquist (1994b, 1996) have shown that galaxies lacking compact bulges tend to suffer prompt inflows when participating in major mergers, while those with centrally condensed bulges do not and are, in fact, better caricatures of the brightest infrared sources. The simulations reported here seem to be intermediate to these two extremes; while our model galaxies do include bulges, they are less concentrated than those employed by Mihos & Hernquist. In this regard, a large parameter survey over orbits and galaxy types would help to expose the key factor(s) that determine the timing of starbursts.

5.3.4. Structure of Elliptical Galaxies

While rather large gas fractions accumulate in the cores of simulated merger remnants (e.g., Fig. 6), these central concentrations amount to no more than $\sim 6\%$ of the luminous material and only $\sim 1.2\%$ of the total mass including dark matter. It is remarkable that such a small amount of dissipative material can cause the marked differences found between the *stellar* components of remnants A and A₀ (e.g., Fig. 17). The results presented here suggest that the gas influences the stellar component by deepening the potential well. Nonetheless, it is not clear how much gas, and what degree of central concentration, is required to produce such effects. If the dynamical effects of central gas concentrations are to resolve apparent kinematic discrepancies between collisionless merger remnants and bright elliptical galaxies (Paper I; Barnes 1995), some physical account of these effects should be given. One possible suggestion (see, e.g., Dubinski 1994) invokes the destabilization of box orbits, otherwise the backbone of a triaxial system, as the gas deepens the potential.

The dense accumulations of gas found in these simulations, converted to stars, would provide a substantial amount of starlight, and these stars should be detectable in real merger products. For example, differences in age and metallicity between the starburst and old stellar populations are expected to produce color and spectral gradients. If the starburst population joins smoothly onto an older stellar background, these gradients might not differ greatly from those that are actually observed (see, e.g., Mihos & Hernquist 1994e). Another possibility, however, is that the star cluster left behind by such a gas concentration would stand out as a luminosity “spike” against the old stellar population (see, e.g., Mihos & Hernquist 1994b). While most elliptical galaxies have luminosity profiles that rise to the smallest radii measured (see, e.g., Kormendy 1987b), few elliptical galaxies appear to possess central spikes as sharp as those that would be produced in our models if all the gas was turned into stars *after* the merger was complete.

In principle, this latter possibility would argue against collisions like those described here as a formation mechanism for normal elliptical galaxies. Indeed, since the dense gas clouds produced in our simulations have masses and radii comparable to the molecular gas concentrations observed in merging starburst systems, the same objection might also be leveled at the proposal by Kormendy & Sanders (1992) that starbursts such as these form elliptical galaxy cores. On the other hand, it is worth asking if the limitations of the simulations might be partly to blame for the luminosity spikes produced in the models. If star formation begins before the cores of the galaxies have completely coalesced, violent relaxation during the last stages of the merger will blend the starburst population in with the preexisting stellar component. Such blending would be even more effective if the bulges of the merging galaxies had rising density profiles at small radii, unlike the rather diffuse and “flabby” cores of the bulges in the present models. In this connection, and in apparent support of the merger hypothesis, some ellipticals *do* show evidence for a central population which seems to be metal rich, possibly young, and kinematically decoupled from the main bodies of these galaxies (see, e.g., Bender & Surma 1992; Davies, Sadler, & Peletier 1993).

5.3.5. Active Galactic Nuclei

Our models may offer a partial explanation for observed correlations between galactic interactions and nuclear activity; the concentration of gas toward the nucleus of a galaxy could plausibly lead to a high accretion rate onto a preexisting nuclear black hole. But the details of this picture have yet to come into focus. Seyfert nuclei often occur in interacting disk galaxies (see, e.g., Osterbrock 1991), and some lower redshift quasars are likewise involved in interactions (see, e.g., Stockton 1990). In many cases, however, these interactions seem to involve smaller satellite galaxies (see, e.g., Bahcall, Kirhakos, & Schneider 1995); it is not clear if such encounters predominate because they are more common or because they are more efficient in producing AGNs. If gas inflows to scales of 0.1–1 kpc are statistically reliable precursors of nuclear activity, the models described here might support the view that AGNs should be no *less* common in equal-mass interactions than they are in encounters with satellite galaxies.

Yet more uncertain is the suggestion that mergers might lead to the *formation*, and not just the refueling, of a central black hole. As Sanders et al. (1988b) note, the spectral energy distributions of ultraluminous infrared galaxies and optical quasars appear to form a continuous sequence. A number of authors have argued that self-gravitating nuclear gas clouds—like, for example, those seen in our models and in ULIR galaxies—might give rise to massive black holes by various processes (see, e.g., Rees 1984; Norman & Scoville 1988; Shlosman, Begelman, & Frank 1990). If so, then ULIR galaxies and quasars may form an evolutionary sequence. But this hypothesis may not be testable until the host galaxies of high-redshift quasars can be adequately studied; given the controversy surrounding the nature of quasar hosts at redshifts of order unity (see, e.g., Bahcall, Kirhakos, & Schneider 1994), it seems unlikely that this question will be settled soon.

Finally, powerful radio sources are often found in elliptical galaxies whose features suggest interactions or even mergers (see, e.g., Schweizer 1980; Heckman et al. 1986;

Vader, Heisler, & Frogel 1989). Such radio galaxies may be powered by the spindown of rotating black holes (see, e.g., Begelman, Blandford, & Rees 1984). There are several ways in which black holes may acquire spin as a result of interactions; for example, a black hole may be spun up by accretion from an external disk, or a pair of black holes on decaying, nearly circular orbits might coalesce to form a single hole with high angular momentum. However, accretion of sufficient mass to impart a significant amount of angular momentum is likely to produce considerable luminosity, so spin-up by disk accretion is only viable if radio galaxies first go through an optically bright phase. On the other hand, a considerable fraction of nearby galaxies appear to contain black holes (see, e.g., Kormendy & Rich-

stone 1995), so the initial conditions assumed by the coalescence scenario do not appear implausible.

This work was supported in part by the Pittsburgh Supercomputing Center, the Alfred P. Sloan Foundation, NASA Theory grants NAGW-2422 and NAG 5-2836, and the National Science Foundation under grants AST 90-18526, ASC 93-18185, and the Presidential Faculty Fellows Program. We thank Jim Bardeen, Tim de Zeeuw, John Dubinski, John Hibbard, Chris Mihos, Martin Rees, David Sanders, François Schweizer, and Alar Toomre for helpful discussions, Joel Welling for assistance in preparing the video, and Kevin Olson for openly and constructively refereeing this paper.

APPENDIX A

The stars and dark matter in our models are governed by the collisionless Boltzmann equation (see, e.g., Binney & Tremaine 1987):

$$\frac{\partial f_k}{\partial t} + \mathbf{v} \cdot \frac{\partial f_k}{\partial \mathbf{r}} - \nabla \phi \cdot \frac{\partial f_k}{\partial \mathbf{v}} = 0, \quad (\text{A1})$$

where $f_k(\mathbf{r}, \mathbf{v}, t) d\mathbf{r} d\mathbf{v}$ is the mass of component k within the phase-space volume $d\mathbf{r} d\mathbf{v}$ centered on the point \mathbf{r}, \mathbf{v} at time t .

The gas in our models obeys the ordinary equations of motion for a compressible fluid, which can be written

$$\frac{\partial \rho}{\partial t} + \nabla \cdot (\rho \mathbf{v}) = 0, \quad (\text{A2})$$

$$\frac{\partial \mathbf{v}}{\partial t} + (\mathbf{v} \cdot \nabla) \mathbf{v} = -\frac{1}{\rho} \nabla P - \nabla \phi, \quad (\text{A3})$$

$$\rho \frac{\partial u}{\partial t} + \rho (\mathbf{v} \cdot \nabla) u + P \nabla \cdot \mathbf{v} = -\mathcal{L}, \quad (\text{A4})$$

where ρ is the gas density, \mathbf{v} is the velocity, P is the pressure, u is the thermal energy per unit mass, and \mathcal{L} is the energy loss function that comprises all nonadiabatic sources and sinks of energy. Two different equations of state are used in these calculations. Most models use an equation of state appropriate for an ideal gas,

$$P = (\gamma - 1) \rho u, \quad (\text{A5})$$

where the ratio of specific heats, γ , was taken equal to 5/3. In one simulation, we adopt an isothermal equation of state

$$P = \rho c_s^2, \quad (\text{A6})$$

where c_s is the (constant) isothermal speed of sound.

Finally, the gravitational field $\phi(\mathbf{r}, t)$ is given by Poisson's equation:

$$\nabla^2 \phi = 4\pi G \rho_{\text{tot}} = 4\pi G \left(\rho + \sum_k \rho_k \right), \quad (\text{A7})$$

where the mass density in component k is

$$\rho_k = \int f_k d\mathbf{v}. \quad (\text{A8})$$

A1. STELLAR DYNAMICS

It is presently not feasible to solve equation (A1) using finite-difference techniques in six dimensions. Instead, we rely on the usual Monte Carlo approach in which phase space is sampled at an initial time to derive particle coordinates \mathbf{r}_i , \mathbf{v}_i and masses m_i for $i = 1, \dots, N$. This N -body representation is then integrated along the characteristic curves of equation (A1):

$$\frac{d\mathbf{r}_i}{dt} = \mathbf{v}_i, \quad \frac{d\mathbf{v}_i}{dt} = -\nabla \phi \Big|_{\mathbf{r}=\mathbf{r}_i}. \quad (\text{A9})$$

In the continuum limit $N \rightarrow \infty$, equations (A9) yield results identical to equation (A1).

A2. GASDYNAMICS

The hydrodynamical equations of motion are solved using a Lagrangian formulation in which the gas is partitioned into fluid elements. By analogy with N -body solutions to the Vlasov equation, a subset of these fluid elements is selected and

represented by particles. In the approach we use, known as smoothed particle hydrodynamics or SPH (Lucy 1977; Gingold & Monaghan 1977), this subset is chosen so that the particle mass density is proportional to the fluid density, ρ . This means that ρ can be estimated from the local density of particles at later times if the system is updated according to the equations of hydrodynamics.

Since the number of particles is finite, it is necessary to introduce a “smoothing” procedure to represent the fields as continuous quantities. For example, if each particle has a mass m_j , the smoothed density is given by

$$\rho(\mathbf{r}) = \sum_{j=1}^N m_j W(\mathbf{r} - \mathbf{r}_j, h), \quad (\text{A10})$$

where $W(\mathbf{r}, h)$ is the smoothing kernel and h is the smoothing length. This interpolation procedure can be generalized in a straightforward manner so that any field can be similarly estimated. We employ the spherically symmetric spline kernel proposed by Monaghan & Lattanzio (1985), for which only particles lying within two smoothing lengths contribute to sums like that in equation (A10). We employ an implementation in which each particle has its own smoothing length. This refinement is necessary in models such as those here since the smoothing length controls the local spatial resolution and steep density gradients develop in the gas as galaxies interact strongly with one another. Smoothing lengths are specified by requiring that each particle have a fixed number of neighbors, \mathcal{N}_s , within a radius $2h$ (Hernquist & Katz 1989). The present results were obtained with $\mathcal{N}_s = 30$. Smoothed estimates are symmetrized using the prescription suggested by Hernquist & Katz (1989).

The smoothed estimate of the density satisfies the continuity equation identically, and thus equation (A2) need not be integrated in time. The coordinates of each particle, i , evolve according to the Lagrangian form of equation (A3)

$$\frac{d\mathbf{r}_i}{dt} = \mathbf{v}_i, \quad \frac{d\mathbf{v}_i}{dt} = -\frac{1}{\rho_i} \nabla P_i + \mathbf{a}_i^{\text{visc}} - \nabla \phi \Big|_{\mathbf{r}=\mathbf{r}_i}. \quad (\text{A11})$$

These expressions are quite similar to the equations of motion for the collisionless particles but include a term to account for pressure gradients and another, $\mathbf{a}_i^{\text{visc}}$, which comprises viscous forces. In our calculations, the smoothed acceleration arising from pressure gradients is evaluated from the symmetric form

$$\frac{1}{\rho_i} \nabla P_i = \sum_j m_j \left(\frac{P_i}{\rho_i^2} + \frac{P_j}{\rho_j^2} \right) \frac{1}{2} [\nabla_i W(\mathbf{r}_i - \mathbf{r}_j, h_j) + \nabla_j W(\mathbf{r}_i - \mathbf{r}_j, h_i)] \quad (\text{A12})$$

(Hernquist & Katz 1989).

Since collisions between galaxies can create strong shocks in the gas, it is necessary to include an artificial viscosity in the equations of motion to maintain stability (Monaghan & Gingold 1983). The runs described here were performed with the symmetric viscous acceleration

$$\mathbf{a}_i^{\text{visc}} = -\sum_j m_j \Pi_{ij} \frac{1}{2} [\nabla_i W(\mathbf{r}_i - \mathbf{r}_j, h_j) + \nabla_j W(\mathbf{r}_i - \mathbf{r}_j, h_i)]. \quad (\text{A13})$$

Most of the simulations employed a form for Π_{ij} suggested by Monaghan (1992):

$$\Pi_{ij} = \frac{-\alpha \mu_{ij} \bar{c}_{ij} + \beta \mu_{ij}^2}{\bar{\rho}_{ij}}, \quad (\text{A14})$$

where

$$\mu_{ij} = \begin{cases} \frac{\mathbf{v}_{ij} \cdot \mathbf{r}_{ij}}{h_{ij}(r_{ij}^2/h_{ij}^2 + \eta^2)} & \text{for } \mathbf{v}_{ij} \cdot \mathbf{r}_{ij} < 0 \\ 0 & \text{for } \mathbf{v}_{ij} \cdot \mathbf{r}_{ij} \geq 0 \end{cases}, \quad (\text{A15})$$

and $\mathbf{r}_{ij} = \mathbf{r}_i - \mathbf{r}_j$, $\mathbf{v}_{ij} = \mathbf{v}_i - \mathbf{v}_j$, $\bar{c}_{ij} = (c_i + c_j)/2$ is the average speed of sound of particles i and j , $h_{ij} = (h_i + h_j)/2$, $\bar{\rho}_{ij} = (\rho_i + \rho_j)/2$, and η prevents numerical divergences. A few experiments were conducted using an alternate form to examine the dependence of our results on the artificial viscosity. Specifically, we tried

$$\Pi_{ij} = \frac{q_i}{\rho_i^2} + \frac{q_j}{\rho_j^2}, \quad (\text{A16})$$

where

$$q_i = \begin{cases} \alpha h_i \rho_i c_i |\nabla \cdot \mathbf{v}|_i + \beta h_i^2 \rho_i |\nabla \cdot \mathbf{v}|_i^2 & \text{for } \nabla \cdot \mathbf{v} < 0 \\ 0 & \text{for } \nabla \cdot \mathbf{v} \geq 0 \end{cases} \quad (\text{A17})$$

with $\nabla \cdot \mathbf{v}$ is estimated according to

$$\nabla \cdot \mathbf{v}_i = -\frac{1}{\rho_i} \sum_{j=1}^N m_j \mathbf{v}_{ij} \cdot \frac{1}{2} [\nabla_i W(\mathbf{r}_{ij}, h_i) + \nabla_j W(\mathbf{r}_{ij}, h_j)] \quad (\text{A18})$$

(see, e.g., Monaghan 1992; Hernquist & Katz 1989). We generally set $\alpha = 0.5$, $\beta = 1.0$, and $\eta^2 = 0.01$. These choices give a reasonable representation of shocks.

The smoothed equation of motion for the specific thermal energy, u , is

$$\frac{du_i}{dt} = \sum_{j=1}^N m_j \frac{1}{2} \left(\frac{P_i}{\rho_i^2} + \frac{P_j}{\rho_j^2} + \Pi_{ij} \right) v_{ij} \cdot \frac{1}{2} [\nabla_i W(r_{ij}, h_i) + \nabla_i W(r_{ij}, h_j)] + \frac{\Gamma - \Lambda}{\rho}, \quad (\text{A19})$$

where $(\Gamma - \Lambda)/\rho$ includes all nonadiabatic processes not associated with the artificial viscosity. For an isothermal equation of state, the sound speed is constant, and it is not necessary to integrate the thermal energy equation.

A3. MICROPHYSICS

The cooling time of interstellar gas is typically much shorter than galactic dynamical times (see, e.g., Spitzer 1978), and so it is not appropriate to ignore the source and sink terms in the thermal energy equation. We model these effects either by adopting an isothermal equation of state or by including heating and cooling terms of the form

$$\Gamma = A n_H + B n_H^2, \quad (\text{A20})$$

$$\Lambda = C n_H^2 (10^{f_1(T)} + 10^{f_2(T)} + 10^{f_3(T)}), \quad (\text{A21})$$

where T is the temperature and n_H is the number density of hydrogen that is related to the gas density by $n_H = X\rho/m_h$ (see, e.g., Hausman 1981). For a gas of cosmic abundance, the hydrogen mass fraction $X = 0.6$ (see, e.g., Clayton 1968). If the gas is not forced to be isothermal, the temperature is computed from the ideal gas law

$$P = \frac{\rho k T}{\mu m_H}, \quad (\text{A22})$$

using equation (A5). For a singly ionized gas of cosmic abundance, the mean molecular weight is $\mu = 0.72$ (see, e.g., Clayton 1968).

The functions $f_1(T)$, $f_2(T)$, and $f_3(T)$ are fitted to conventional cooling curves for interstellar gas (see, e.g., Dalgarno & McCray 1972; Spitzer 1978; Hausman 1981), and the constant C appearing in equation (A21) has the value $C = 10^{-21}$ ergs $\text{cm}^3 \text{s}^{-1}$. The heating terms in equation (A20) are chosen to provide a phenomenological description of a two-phase medium by setting $A = 7.82 \times 10^{-27}$ ergs s^{-1} and $B = 1.98 \times 10^{-27}$ ergs $\text{cm}^3 \text{s}^{-1}$. The balance between heating and cooling would then yield two states in pressure equilibrium with total number densities of free particles and temperatures $n_1 = 0.5 \text{ cm}^{-3}$, $T_1 = 8000 \text{ K}$ and $n_2 = 50 \text{ cm}^{-3}$, $T_2 = 80 \text{ K}$, respectively. Owing to numerical limitations, we are also forced to impose a lower limit to the cooling function so that the gas cannot cool by radiative processes to less than 10^4 K , to inhibit local instabilities in the gas. Thus, we cannot accurately predict the distribution of molecular gas in our models. For simplicity, effects related to star formation and supernovae are ignored.

A4. TIME INTEGRATION

Particle positions and velocities are updated using a time-centered leapfrog integrator, supplemented by correction terms when positions and velocities are synchronized (Hernquist & Katz 1989). Thermal energies are advanced along with positions and equation (A19) is integrated semi-implicitly using a trapezoidal rule. Particles have their own time steps, which are power-of-2 subdivisions of the largest system time step, implying that the code is temporally adaptive (Hernquist & Katz 1989). The time steps for the gas particles are chosen to satisfy a version of the Courant condition modified to include viscous effects (Hernquist & Katz 1989). In the simulations presented here, the Courant number has the value $\mathcal{C} = 0.3$.

A5. GRAVITATIONAL FORCES

The gravitational potential is computed using a hierarchical tree algorithm, employing a recursive partition of space into nested cubes (Barnes & Hut 1986). In this scheme, the potential from distant cubes is approximated by low-order multipole expansions, in such a manner that the force on N particles can be obtained in $O(N \log N)$ operations. It should be emphasized that tree codes do not suffer from relaxation effects more severely than other N -body codes (Hernquist & Barnes 1990; Hernquist & Ostriker 1992), contrary to claims that appear occasionally in the literature.

Several refinements have been incorporated into our tree code, such as quadrupole corrections to improve the accuracy of the gravitational field (Hernquist 1987) and efficient vectorizations of the force calculation procedure (see, e.g., Barnes 1990; Hernquist 1990c). The simulations described here were performed with an accuracy parameter $\theta = 0.7$, including quadrupole corrections to the force calculation and using the vectorization scheme suggested by Hernquist (1990c), which is optimized for Crays. On small scales, the gravitational interaction is softened using a cubic spline (Hernquist & Katz 1989).

A6. IMPLEMENTATION DETAILS

Since the smoothed estimates used to compute local hydrodynamic properties involve only particles within two smoothing lengths of a given point, an efficient algorithm for performing nearest neighbor searches is required. We determine nearest neighbors with the same tree structure used to compute gravitational forces, an approach that is especially effective when smoothing lengths are variable, as in our code.

All aspects of tree construction, force calculation, and nearest neighbor searching are full vectorizable. Even so, numerical results like those presented here typically require of order 10–20 cpu hr on a Cray Y-MP, like the one at the Pittsburgh Supercomputing Center where the simulations were performed.

APPENDIX B

The five video sequences that are related to this paper and will appear on a videotape with a later issue of *The Astrophysical Journal* are briefly described here.

1. **Encounter Overview.** This sequence shows the time evolution of encounter A, viewed along the orbital axis. Here, dark halo matter is shown in red, bulge stars are shown in yellow, disk stars are shown in blue, and the gas is shown in green.
2. **Gas Only.** This sequence also views encounter A along the orbital axis, but at a larger scale. Moreover, here only the gas in the two galaxies is shown.
3. **Disk Response.** In this sequence the direct disk from encounter A is viewed along its spin axis, using the same color scheme as in section 1.
4. **Final Encounter.** This sequence presents up a close-up of the latter part of section 2, using the same color scheme.
5. **Dwarf Formation.** This sequence shows the formation of the most massive bound object in the tidal tails of encounter A. Here stars and gas that wind up in the “dwarf” are shown in blue and green, respectively, while other disk and bulge stars are shown in red; halo matter is not shown.

REFERENCES

- Allen, D. A., Roche, P. F., & Norris, R. P. 1985, *MNRAS*, 213, 67P
 Armus, L., Heckman, T. M., & Miley, G. 1987, *AJ*, 94, 831
 Athanassoula, E. 1992, *MNRAS*, 259, 345
 Baan, W. A., Haschick, A. D., & Henkel, C. 1989, *ApJ*, 346, 680
 Bahcall, J. N., Kirhakos, S., & Schneider, D. T. 1994, *ApJ*, 435, L11
 ———. 1995, *ApJ*, 447, L1
 Bahcall, J. N., & Soneira, R. M. 1980, *ApJS*, 44, 73
 Balcells, M., & Quinn, P. J. 1990, *ApJ*, 361, 381
 Barnes, J. 1988, *ApJ*, 331, 699
 ———. 1990, *J. Comp. Phys.*, 87, 161
 ———. 1992, *ApJ*, 393, 484 (Paper I)
 ———. 1995, in *The Formation and Evolution of Galaxies*, ed. C. Munoz-Tunon & F. Sanchez (Cambridge: Cambridge Univ. Press), 399
 Barnes, J., & Hernquist, L. 1991, *ApJ*, 370, L65 (BH91)
 ———. 1992, *Nature*, 360, 715
 ———. 1993, *Phys. Today*, 46(3), 54
 Barnes, J., & Hut, P. 1986, *Nature*, 324, 446
 Begelman, M. C., Blandford, R. D., & Rees, M. J. 1984, *Rev. Mod. Phys.*, 56, 225
 Bender, R. 1990a, in *Dynamics and Interactions of Galaxies*, ed. R. Wielen (Heidelberg: Springer), 232
 ———. 1990b, *A&A*, 229, 441
 Bender, R., & Surma, P. 1992, *A&A*, 258, 250
 Binney, J., & Tremaine, S. 1987, *Galactic Dynamics* (Princeton: Princeton Univ. Press)
 Carlberg, R. 1986, *ApJ*, 310, 593
 Carlberg, R., & Freedman, W. L. 1985, *ApJ*, 298, 486
 Clayton, D. D. 1968, *Principles of Stellar Evolution and Nucleosynthesis* (New York: McGraw-Hill)
 Colina, L., Lipari, S., & Macchetto, F. 1991, *ApJ*, 379, 113
 Combes, F., Dupraz, C., & Gerin, M. 1990, in *Dynamics and Interactions of Galaxies*, ed. R. Wielen (Berlin: Springer), 205
 Dalgarno, A., & McCray, R. A. 1972, *ARA&A*, 10, 375
 Davies, R. L., Sadler, E. M., & Peletier, R. F. 1993, *MNRAS*, 262, 650
 de Vaucouleurs, G. 1948, *Ann. d'Ap.*, 11, 247
 de Zeeuw, P. T. 1985a, *MNRAS*, 215, 731
 ———. 1985b, *MNRAS*, 216, 273
 Dubinski, J. 1994, *ApJ*, 431, 617
 Dubinski, J., & Carlberg, R. G. 1991, *ApJ*, 378, 496
 Elmegreen, B. G., Kaufman, M., & Thomasson, M. 1993, *ApJ*, 412, 90
 Forbes, D. A., Franx, M., & Illingworth, G. D. 1995, *AJ*, 109, 1988
 Franx, M., & Illingworth, G. 1988, *ApJ*, 327, L55
 Gerola, H., Carnevali, P., & Salpeter, E. E. 1983, *ApJ*, 268, L75
 Gingold, R. A., & Monaghan, J. J. 1977, *MNRAS*, 181, 375
 Hausman, M. A. 1981, *ApJ*, 245, 72
 Heckman, T. M., Armus, L., & Miley, G. K. 1990, *ApJS*, 74, 833
 Heckman, T. M., Smith, E. P., Baum, S. A., van Breugel, W. J. M., Miley, G. K., Illingworth, G. D., Bothun, G. D., & Balick, B. 1986, *ApJ*, 311, 526
 Hernquist, L. 1987, *ApJS*, 64, 715
 ———. 1989a, *Nature*, 340, 687
 ———. 1989b, *Ann. NY Acad. Sci.*, 571, 190
 ———. 1990a, in *Dynamics and Interactions of Galaxies*, ed. R. Wielen (Berlin: Springer), 108
 ———. 1990b, *ApJ*, 356, 359
 ———. 1990c, *J. Comput. Phys.*, 87, 137
 ———. 1991, *Int. J. Supercomput. Appl.*, 5, 71
 ———. 1992, *ApJ*, 400, 460
 ———. 1993a, *ApJ*, 409, 548
 ———. 1993b, *ApJ*, 404, 717
 Hernquist, L., & Barnes, J. 1990, *ApJ*, 349, 562
 ———. 1991, *Nature*, 354, 210
 Hernquist, L., & Katz, N. 1989, *ApJS*, 70, 419
 Hernquist, L., & Mihos, J. C. 1995, *ApJ*, 448, 41
 Hernquist, L., & Ostriker, J. P. 1992, *ApJ*, 386, 375
 Hernquist, L., & Quinn, P. J. 1988, *ApJ*, 331, 682
 ———. 1989, *ApJ*, 342, 1
 Hernquist, L., & Spergel, D. N. 1992, *ApJ*, 399, L117
 Hernquist, L., Spergel, D. N., & Heyl, J. S. 1993, *ApJ*, 416, 415
 Hernquist, L., & Weil, M. L. 1992, *Nature*, 358, 734
 ———. 1993, *MNRAS*, 261, 804
 Heyl, J. S., Hernquist, L., & Spergel, D. N. 1994, *ApJ*, 427, 165
 Hibbard, J., Guhathakurta, P., van Gorkom, J. H., & Schweizer, F. 1994, *AJ*, 107, 67
 Hibbard, J., & Mihos, J. C. 1995, *AJ*, 110, 140
 Jedrzejewski, R., & Schechter, P. L. 1988, *ApJ*, 330, L87
 Joseph, R. D., & Wright, G. S. 1985, *MNRAS*, 214, 87
 Katz, N. 1991, *ApJ*, 368, 325
 ———. 1992, *ApJ*, 391, 502
 Katz, N., & Gunn, J. E. 1991, *ApJ*, 377, 365
 King, I. R. 1966, *AJ*, 71, 64
 Kleinmann, S. G., et al. 1988, *ApJ*, 328, 161
 Kormendy, J. 1984, *ApJ*, 287, 577
 ———. 1987a, in *Dark Matter in the Universe*, ed. J. Kormendy & G. R. Knapp (Dordrecht: Reidel), 139
 ———. 1987b, in *Structure and Dynamics of Elliptical Galaxies*, ed. P. T. de Zeeuw (Dordrecht: Reidel), 17
 Kormendy, J., & Richstone, D. O. 1995, *ARA&A*, 33, 581
 Kormendy, J., & Sanders, D. B. 1992, *ApJ*, 390, L53
 Lake, G. 1989, *AJ*, 97, 1312
 Larson, R. B. 1987, in *Starbursts and Galaxy Evolution*, ed. T. X. Thuan, T. Montmerle, J. T. T. Van (Gif sur Yvette: Editions Frontieres), 467
 Larson, R. B., & Tinsley, B. M. 1978, *ApJ*, 219, 46
 Lucy, L. 1977, *AJ*, 82, 1013
 McKee, C. F., & Ostriker, J. P. 1977, *ApJ*, 218, 198
 Mihos, J. C., Bothun, G. D., & Richstone, D. O. 1993, *ApJ*, 418, 82
 Mihos, J. C., & Hernquist, L. 1994a, *ApJ*, 425, L13
 ———. 1994b, *ApJ*, 431, L9
 ———. 1994c, *ApJ*, 427, 112
 ———. 1994d, *ApJ*, 437, 611
 ———. 1994e, *ApJ*, 427, 112
 ———. 1996, *ApJ*, 464, 641
 Miralda-Escudé, J., & Schwarzschild, M. 1989, *ApJ*, 339, 752
 Mirabel, I. F., Dottori, H., & Lutz, D. 1992, *A&A*, 256, L19
 Mirabel, I. F., Lutz, D., & Maza, J. 1991, *A&A*, 243, 367
 Monaghan, J. J. 1992, *ARA&A*, 30, 543
 Monaghan, J. J., & Gingold, R. A. 1983, *J. Comp. Phys.*, 52, 374
 Monaghan, J. J., & Lattanzio, J. C. 1985, *A&A*, 149, 135
 Mould, J. 1992, in *The Astronomy and Astrophysics Encyclopedia*, ed. S. P. Maran (New York: Nostrand-Reinhold), 238
 Navarro, J., & White, S. D. M. 1993, *MNRAS*, 265, 271
 Negroponte, J., & White, S. D. M. 1983, *MNRAS*, 205, 1009
 Nelson, R. P., & Papaloizou, J. C. B. 1994, *MNRAS*, 270, 1
 Nicholson, R. A., Bland-Hawthorn, J., & Taylor, K. 1992, *ApJ*, 387, 503
 Noguchi, M. 1987, *MNRAS*, 228, 635
 Noguchi, M. 1988, *A&A*, 203, 259
 Noguchi, M., & Ishibashi, S. 1986, *MNRAS*, 219, 305
 Norman, C., & Scoville, N. 1988, *ApJ*, 332, 124
 Olson, K. M., & Kwan, J. 1990a, *ApJ*, 349, 480
 ———. 1990b, *ApJ*, 361, 426
 Osterbrock, D. E. 1991, *Rep. Prog. Phys.*, 54, 579
 Pryor, C. 1992, in *Morphological and Physical Classification of Galaxies*, ed. G. Longo et al. (Dordrecht: Kluwer), 163
 Quinn, P. J. 1984, *ApJ*, 279, 596
 Rees, M. J. 1984, *ARA&A*, 22, 471
 Rix, H.-W., & White, S. D. M. 1992, *MNRAS*, 254, 389
 Sanders, D. B. 1992, in *ASP Conf. Proc. 31, Relationships between Active Galactic Nuclei and Starburst Galaxies*, ed. A. V. Filippenko (San Francisco: ASP), 303
 Sanders, D. B., & Mirabel, I. F. 1985, *ApJ*, 298, L31
 Sanders, D. B., et al. 1986, *ApJ*, 305, L45
 Sanders, D. B., Scoville, N. Z., Sargent, A. I., & Soifer, B. T. 1988a, *ApJ*, 324, L55

- Sanders, D. B., Soifer, B. T., Elias, J. H., Madore, B. F., Mathews, K., Neugebauer, G., & Scoville, N. Z. 1988b, *ApJ*, 325, 74
- Sanders, D. B., Scoville, N. Z., & Soifer, B. T. 1991, *ApJ*, 370, 158
- Sanders, D. B., Young, J. S., Scoville, N. Z., Soifer, B. T., & Danielson, G. E. 1987, *ApJ*, 312, L5
- Sargent, A. I., Sanders, D. B., Scoville, N. Z., & Soifer, B. T. 1987, *ApJ*, 312, L35
- Sargent, A. I., Sanders, D. B., & Phillips, T. G. 1989, *ApJ*, 346, L9
- Schiminovich, D., van Gorkom, J. H., van der Hulst, J. M., & Kasow, S. 1994, *ApJ*, 423, L101
- Schwarz, M. P. 1984, *MNRAS*, 209, 93
- Schweizer, F. 1978, in *Structure and Properties of Nearby Galaxies*, ed. E. M. Berkhuijsen & R. Wielebinski (Dordrecht: Reidel), 279
- Schweizer, F. 1980, *ApJ*, 237, 303
- . 1982, *ApJ*, 252, 455
- . 1986, *Science*, 231, 227
- . 1990, in *Dynamics and Interactions of Galaxies*, ed. R. Wielen (Berlin: Springer), 60
- Scoville, N. Z. 1992, in *ASP Conf. Proc. 31, Relationships between Active Galactic Nuclei and Starburst Galaxies* ed. A. V. Filippenko (San Francisco: ASP), 159
- Scoville, N. Z., Sanders, D. B., Sargent, A. I., Soifer, B. T., Scott, S. L., & Lo, K. Y. 1986, *ApJ*, 311, L42
- Scoville, N. Z., Sargent, A. I., Sanders, D. B., & Soifer, B. T. 1991, *ApJ*, 366, L5
- Seitzer, P., & Schweizer, F. 1990, in *Dynamics and Interactions of Galaxies*, ed. R. Wielen (Berlin: Springer), 270
- Sellwood, J. A. 1989, in *Dynamics of Astrophysical Disks*, ed. J. A. Sellwood (Cambridge: Cambridge Univ. Press), 155
- Sellwood, J. A., & Carlberg, R. G. 1984, *ApJ*, 282, 61
- Shier, L. M., Rieke, M. J., & Rieke, G. H. 1994, *ApJ*, 433, L9
- Shlosman, I., Begelman, M. C., & Frank, J. 1990, *Nature*, 345, 679
- Soifer, B. T., et al. 1984a, *ApJ*, 278, L71
- Soifer, B. T., et al. 1984b, *ApJ*, 283, L1
- Solomon, P. M., Downes, D., & Radford, S. J. E. 1992, *ApJ*, 387, L55
- Spitzer, L. 1978, *Physical Processes in the Interstellar Medium* (New York: Wiley)
- Steiman-Cameron, T. Y., Kormendy, J., & Durisen, R. H. 1992, *AJ*, 104, 1339
- Stockton, A. 1974, *ApJ*, 187, 219
- . 1990, in *Dynamics and Interactions of Galaxies*, ed. R. Wielen (Berlin: Springer), 440
- Tinney, C. G., Scoville, N. Z., Sanders, D. B., & Soifer, B. T. 1990, *ApJ*, 362, 471
- Toomre, A. 1981, in *The Structure and Evolution of Normal Galaxies*, ed. S. M. Fall & D. Lynden-Bell (Dordrecht: Reidel), 111
- . 1990, in *Dynamics and Interactions of Galaxies*, ed. R. Wielen (Berlin: Springer), 292
- Toomre, A., & Toomre, J. 1972, *ApJ*, 179, 623
- Urby, S. 1993, *A&A*, 268, 35
- Vader, J. P., Heisler, C. A., & Frogel, J. A. 1989, *Ann. NY Acad. Sci.*, 571, 247
- van Gorkom, J. H., van der Hulst, J. M., Haschick, A. D., & Tubbs, A. D. 1990, *AJ*, 99, 1781
- Vedel, H., & Sommer-Larsen, J. 1990, *MNRAS*, 245, 637
- Wallin, J. F. 1990, *AJ*, 100, 1477
- Young, J. S., Kenney, J., Lord, S. D., & Schloerb, F. P. 1984, *ApJ*, 287, L65
- Young, J. S., Schloerb, F. P., Kenney, J., & Lord, S. D. 1986, *ApJ*, 304, 443
- Zwicky, F. 1956, *Egeb. Exakt. Naturwiss.* 29, 344